

ALMA observations of NGC 6334S – I:  
Forming massive stars and cluster in subsonic and transonic filamentary clouds

SHANGHUO LI,<sup>1,2,3</sup> QIZHOU ZHANG,<sup>2</sup> HAUYU BAOBAB LIU,<sup>4</sup> HENRIK BEUTHER,<sup>5</sup> AINA PALAU,<sup>6</sup> JOSEP MIQUEL GIRART,<sup>7</sup>  
HOWARD SMITH,<sup>2</sup> JOSEPH L. HORA,<sup>2</sup> YUXING LIN,<sup>8</sup> KEPING QIU,<sup>9</sup> SHAYE STROM,<sup>2</sup> JUNZHI WANG,<sup>1</sup> FEI LI,<sup>1,3</sup> AND  
NANNAN YUE<sup>10,3</sup>

<sup>1</sup>*Shanghai Astronomical Observatory, Chinese Academy of Sciences, 80 Nandan Road, Shanghai 200030, China*

<sup>2</sup>*Center for Astrophysics | Harvard & Smithsonian, 60 Garden Street, Cambridge, MA 02138, USA*

<sup>3</sup>*University of Chinese Academy of Sciences, 19A Yuquanlu, Beijing 100049, China*

<sup>4</sup>*Academia Sinica Institute of Astronomy and Astrophysics, P.O. Box 23-141, Taipei 106, Taiwan*

<sup>5</sup>*Max Planck Institute for Astronomy, Königstuhl 17, 69117 Heidelberg, Germany*

<sup>6</sup>*Instituto de Radioastronomía y Astrofísica, Universidad Nacional Autónoma de México, P.O. Box 3-72, 58090, Morelia, Michoacán, México*

<sup>7</sup>*Institut de Ciències de l'Espai (IEEC-CSIC), Campus UAB, Carrer de Can Magrans s/n, 08193 Cerdanyola del Vallès, Catalonia, Spain*

<sup>8</sup>*Max-Planck Institute für Radio Astronomy, Auf dem Hügel 69, 53121, Bonn, Germany*

<sup>9</sup>*School of Astronomy and Space Science, Nanjing University, 163 Xianlin Avenue, Nanjing 210023, China*

<sup>10</sup>*National Astronomical Observatories, Chinese Academy of Sciences, Beijing 100012*

## ABSTRACT

We present Atacama Large Millimeter/submillimeter Array (ALMA) and Karl G. Jansky Very Large Array (JVLA) observations of the massive infrared dark cloud NGC 6334S (also known as IRDC G350.56+0.44), located at the southwestern end of the NGC 6334 molecular cloud complex. The H<sup>13</sup>CO<sup>+</sup> and the NH<sub>2</sub>D lines covered by the ALMA observations at a  $\sim 3''$  angular resolution ( $\sim 0.02$  pc) reveal that the spatially unresolved non-thermal motions are predominantly subsonic and transonic, a condition analogous to that found in low-mass star-forming molecular clouds. The observed supersonic non-thermal velocity dispersions in massive star forming regions, often reported in the literature, might be significantly biased by poor spatial resolutions that broaden the observed line widths due to unresolved motions within the telescope beam. Our 3 mm continuum image resolves 49 dense cores, whose masses range from 0.17 to 14  $M_{\odot}$ . The majority of them are resolved with multiple velocity components. Our analyses of these gas velocity components find an anti-correlation between the gas mass and the virial parameter. This implies that the more massive structures tend to be more gravitationally unstable. Finally, we find that the external pressure in the NGC 6334S cloud is important in confining these dense structures, and may play a role in the formation of dense cores, and subsequently, the embedded young stars.

*Keywords:* Early-type stars (430), Star formation (1569), Massive stars (732), Protoclusters (1297), Protostars (1302), Radio spectroscopy (1359), Radio continuum emission (1340), Radio interferometers (1345), Submillimeter astronomy (1647), Molecular spectroscopy (2095)

## 1. INTRODUCTION

Molecular clouds in the Milky Way are in general inefficient in forming stars ( $\sim 1\%$ , Myers et al. 1986; Murray 2011; Vutisalchavakul et al. 2016), an observation that has motivated the long-standing hypotheses that they are supported by supersonic turbulence or mag-

netic fields against their self-gravitational collapse (for the review see Vazquez-Semadeni et al. 2000; Mac Low & Klessen 2004; Bergin & Tafalla 2007; McKee & Ostriker 2007). Larson (1981) reported an empirical, positive correlation between the physical size scale and the velocity dispersion of molecular clouds. Although the study was based on measurements from different clouds, this correlation has been taken as indications that turbulence dissipates toward smaller spatial scales where gas is prone to the gravitational collapse and the subsequent

star-formation (see Bonazzola et al. 1987; Stone et al. 1998; Mac Low et al. 1998; Mac Low & Klessen 2004; Krumholz & McKee 2005; Elmegreen & Scalo 2004; Hennebelle & Chabrier 2008, and references therein). As a consequence, on spatial scales of dense star-forming cores ( $\lesssim 0.1$  pc), the non-thermal motions may be sonic (Myers & Goodman 1988; Goodman et al. 1998; Caselli et al. 2002). This is consistent with the observations of some filamentary, low-mass star-forming clouds (e.g., Hacar & Tafalla 2011; Hacar et al. 2013; Pineda et al. 2015; Hacar et al. 2016b, 2017).

In contrast, previous observations towards high-mass star-forming regions have reported supersonic non-thermal velocity dispersion (Caselli & Myers 1995; Pirogov et al. 2003; Shirley et al. 2003; Wang et al. 2008; Vasyunina et al. 2011; Sanhueza et al. 2012; Li et al. 2017). The formation of gas cores of high mass and high density may be supported by supersonic turbulence. Otherwise they may fragment to form lower-mass stars since their masses are much larger than the Jeans mass (McKee & Tan 2003). However, recent higher angular resolution observations started to reveal subsonic non-thermal velocity dispersion in massive star-forming molecular clouds on small spatial scales (e.g., Beuther et al. 2018; Hacar et al. 2018; Monsch et al. 2018; Sokolov et al. 2018). Whether the massive star- and cluster-forming regions are initially supported by supersonic turbulence remains a matter of debate, and needs to be clarified with more observations of target sources at early evolutionary stages.

Using the Atacama Large Millimeter Array (ALMA) and the Karl G. Jansky Very Large Array (JVLA), we have carried out high angular resolution observations towards the infrared dark, massive cluster-forming molecular cloud NGC 6334S, which is located at the southwestern end of the NGC 6334 molecular cloud complex. In contrast to the other luminous OB cluster-forming clumps in the NGC 6334 molecular cloud complex, namely the I, I(N), II, III, IV, and V clumps (Persi & Tapia 2008; Russeil et al. 2013; Willis et al. 2013), NGC 6334S is dark at IR wavelengths and lacks signs of massive star formation (see Figure 1). With a mass of  $1.3 \times 10^3 M_{\odot}$ , comparable to the clumps with embedded massive protostars and protocluster in the complex, NGC 6334S has the potential to form massive stars with a cluster of lower mass objects. The proximity of NGC 6334S ( $d \sim 1.3$  kpc; Chibueze et al. 2014) makes it an ideal laboratory to investigate the key physical processes related to massive star and cluster formation.

In this paper, we investigate the dynamical motions of identified embedded dense cores and their parent cloud, as well as the dynamical stability of dense cores. First,

we describe our ALMA and JVLA observations in § 2. Then, we present the results and analysis in § 3. We discuss in detail the properties of dense cores and their parent cloud in § 4. Finally, we summarize the conclusion of this work in § 5.

## 2. OBSERVATIONS

### 2.1. ALMA Observations

We carried out a 55-pointings mosaic of the massive infrared dark cloud (IRDC), NGC 6334S, between 2017 March 13 and 2017 March 21 using the 12-m main array of ALMA (ID: 2016.1.00951.S, PI: Shaye Strom). The overall observing time and the on-source integration time are 7.3 hours and 4.4 hours, respectively. The projected baseline lengths range from 15 to 155 meters ( $\sim 4.9$ -51 k $\lambda$  at the averaged frequency of 98.5 GHz).

We employed two 234.4 MHz wide spectral windows to cover the  $\text{H}^{13}\text{CO}^+$  1-0 (86.754 GHz) and  $\text{NH}_2\text{D}$   $1_{11}-1_{01}$  (85.926 GHz) lines, respectively, with a spectral resolution of 61 kHz ( $\sim 0.21$  km s $^{-1}$  at 86 GHz). In addition, we centered three 1.875 GHz wide spectral windows at 88.5 GHz, 98.5 GHz, and 100.3 GHz to obtain broad band continuum data. We observed the quasars J1617-5858, J1713-3418, and J1733-1304, for passband, complex gain, and absolute flux calibrations, respectively.

The data calibrations were performed by the supporting staff at the ALMA Regional Center (ARC), using the CASA software package (McMullin et al. 2007). The continuum image was obtained using the three 1.875 GHz spectral windows with a Briggs’s robust weighting of 0.5 to the visibilities. This yields a synthesized beam of  $3''.6 \times 2''.4$  (or  $0.023 \times 0.015$  pc) with a position angle (P.A.) of  $81^\circ$  and a  $1\sigma$  root mean square (rms) noise level of  $0.03$  mJy beam $^{-1}$ . For both  $\text{H}^{13}\text{CO}^+$  and  $\text{NH}_2\text{D}$  lines, we used a Briggs’s robust weighting of 0.5 to the visibilities, which achieved a synthesized beam of about  $4''.1 \times 2''.8$  (PA=  $83^\circ$ , or  $0.026 \times 0.018$  pc) for these two lines. The  $1\sigma$  rms noise level is about  $6$  mJy beam $^{-1}$  per  $0.21$  km s $^{-1}$  channel for both the  $\text{H}^{13}\text{CO}^+$  and  $\text{NH}_2\text{D}$  lines.

### 2.2. JVLA Observations

We carried out a 4-pointings mosaic of the central region of NGC 6334S using the JVLA, on 2014 August 28 (project code: 14A-241; PI: Qizhou Zhang). These observations simultaneously covered the  $\text{NH}_3$  (1,1) through (5,5) metastable inversion transitions. The overall observing time was 2 hours, which yielded an on-source integration of  $\sim 20$  minutes for each pointing. The Quasars 3C286, J1743-0350 and J1744-3316 were observed for flux, bandpass and gain calibrations, respectively.

The data calibration and imaging were carried out using the CASA software package. Our target source is located in the south, which leads to shorter projected baselines in the north-south direction. To increase the signal-to-noise (S/N) ratio, we tapered the visibilities with an elliptical Gaussian with full width at half-maximum (FWHM) of  $6'' \times 3''$  (P.A. =  $0^\circ$ ). The achieved synthesized beam size is about  $10'' \times 5''$  (P.A. =  $26^\circ$ , or  $0.063 \times 0.032$  pc) for the  $\text{NH}_3$  (1,1) and (2,2) lines. The continuum image achieved a  $1\sigma$  rms noise of  $30 \mu\text{Jy beam}^{-1}$ , while spectral line images achieved a  $1\sigma$  rms noise of  $9 \text{ mJy beam}^{-1}$  at a spectral resolution of  $0.2 \text{ km s}^{-1}$ .

### 2.3. Fitting molecular line spectra

We fit Gaussian line profiles to the  $\text{H}^{13}\text{CO}^+$  image cube pixel by pixel, using the `PySpecKit` package (Ginsburg & Mirocha 2011). We excluded regions where the peak intensity in the spectral domain is below 5 times the rms noise level. For data above the cutoff, we regarded spectral peaks that are separated by more than 2 spectral channels and brighter than 5 times the rms noise level as independent velocity components. We then simultaneously fit Gaussian profiles to all of the independent velocity components. We eliminated poor fits by only keeping pixels that fulfill the following criteria: (1)  $\sigma_{\text{obs}} > 3\Delta\sigma_{\text{obs}}$ , which ensures that the derived observed velocity dispersion is reliable. (2)  $-8 \leq v_{\text{lsr}} \leq 0 \text{ km s}^{-1}$ , which is the  $\text{H}^{13}\text{CO}^+$  line emission velocity range in the NGC 6334S. (3)  $I > 3\Delta_I$ . (In these criteria,  $\Delta\sigma_{\text{obs}}$  is the uncertainty of the observed velocity dispersion  $\sigma_{\text{obs}}$ ,  $v_{\text{lsr}}$  is the central velocity, and  $\Delta_I$  is the uncertainty of velocity integrated intensity  $I$ .) The observed velocity dispersion,  $\sigma_{\text{obs}}$ , is the combination of both thermal and non-thermal velocity dispersion values. The  $\text{NH}_2\text{D}$  line cubes were fit following a similar routine but including its 36 hyperfine components (Daniel et al. 2016).

The  $\text{NH}_3$  (1,1) and (2,2) transitions were jointly fit, pixel by pixel, using `PySpecKit` in order to estimate the gas kinetic temperature and the line width. Details of the procedure have been provided in Friesen et al. (2017). Limited by S/N ratios, we cannot robustly fit multiple velocity components to the  $\text{NH}_3$  spectra. Nevertheless, for our purpose of deriving the gas temperature and assessing the uncertainty of converting the  $\text{NH}_3$  rotational temperature to the gas kinetic temperature, it is adequate to assume a single velocity component. We have compared the gas temperatures estimated from  $\text{NH}_3$  and dust temperatures estimated by SED fitting the PACS  $160 \mu\text{m}$ , SPIRE  $250 \mu\text{m}$ , PLANCK and ATLASGAL  $870 \mu\text{m}$  data (see Appendix A). In spite of the different angular resolutions, we found that the derived gas and dust temperatures are consistent to within  $\leq 3$

K at the central part of NGC 6334S, and are consistent to around 6 K over a more extended area (Figure 2). We use a uniform temperature of  $\langle T_{\text{NH}_3} \rangle = 15 \text{ K}$ , the averaged temperature from the  $\text{NH}_3$  data, to calculate the gas masses, thermal line widths and the sound speeds for the regions where the  $\text{NH}_3$  data are not available (see Section 3.3 and Section 3.4).

## 3. RESULTS AND ANALYSIS

The present work focuses on the non-thermal velocity dispersion of the NGC 6334S cloud and the embedded dense cores, as well as the stability of the dense cores. Both  $\text{H}^{13}\text{CO}^+$  1-0 (critical density,  $n_{\text{cr}} \sim 2 \times 10^4 \text{ cm}^{-3}$ ) and  $\text{NH}_2\text{D}$   $1_{11}\text{-}1_{01}$  ( $n_{\text{cr}} \sim$  a few  $10^5 \text{ cm}^{-3}$ ) are good dense gas tracers in star formation regions (e.g., Pillai et al. 2007; Busquet et al. 2010; Sanhueza et al. 2012), which allows us to investigate the kinematic properties on spatial scales of both molecular cloud and dense cores. The  $\text{H}^{13}\text{CO}^+$  molecule ( $\mu = 30$ ,  $\sigma_{\text{th}(15\text{K})} = 0.06 \text{ km s}^{-1}$ ) has a higher molecular weight than the  $\text{NH}_2\text{D}$  molecule ( $\mu = 18$ ,  $\sigma_{\text{th}(15\text{K})} = 0.08 \text{ km s}^{-1}$ ), and therefore is a better probe of the non-thermal gas motions. In spite of the hyperfine line splitting of the  $\text{H}^{13}\text{CO}^+$  1-0 transitions with six components, they are closer than  $0.14 \text{ km s}^{-1}$  (41 kHz) at the frequency of the  $\text{H}^{13}\text{CO}^+$  1-0 line (Schmid-Burgk et al. 2004). The averaged line width reduction is about  $0.01 \text{ km s}^{-1}$  when the hyperfine structure of the  $\text{H}^{13}\text{CO}^+$  is fully taken into account, which is much smaller than the derived line widths (Section 3.3). Therefore, the hyperfine components of the  $\text{H}^{13}\text{CO}^+$  1-0 can be treated as the same transition for our analysis. The main hyperfine line components of the  $\text{NH}_2\text{D}$  1-1 line are resolved by the observations, which permits robustly deriving the line widths towards the localized cores with higher gas column densities (e.g., Pillai et al. 2011). When there are multiple velocity components along the line-of-sight, they can be confused with the hyperfine line structures of the  $\text{NH}_2\text{D}$ . Nevertheless, this issue can be mitigated by comparing them with the spectrum of the  $\text{H}^{13}\text{CO}^+$  line. Finally, the multiple inversion line transitions of  $\text{NH}_3$  can be simultaneously covered by the observations of JVLA thanks to its broad bandwidth capability.

### 3.1. Dense core identification

We employed the `astrodendro`<sup>1</sup> algorithm to pre-select dense cores (i.e., the leaves in the terminology of `astrodendro`) from the 3 mm continuum image (Figure 1). The specific properties of the dense cores (size, flux density, peak intensity and position) iden-

<sup>1</sup> <http://dendrograms.org/>

tified from the `astrodendro` analysis are obtained using the `CASA-imfit` task. There are some compact sources that are detected at  $> 5\sigma$  significance but missed by `astrodendro`; we use `CASA-imfit` to recover them from the image. We avoid identifying sources from the elongated filament southeast of NGC 6334S (Figure 1). This elongated filament is not detected with spectral line emission counterpart, and is likely dominated by free-free or synchrotron emission and likely associated with the HII region east of this filament. When computing the dendrogram the following parameters are used: the minimum pixel value `min_value` =  $3\sigma$ , where  $\sigma$  is the rms noise of continuum image; the minimum difference in the peak intensity between neighboring compact structures `min_delta` =  $1\sigma$ ; the minimum number of pixels required for a structure to be considered an independent entity `min_npix` = 40, which is approximately the synthesized beam area.

We identified 49 dense cores (Table 1), which are labelled in Figure 1 and presented as pink stars in Figure 3. They are closely associated with gas filamentary structures, and the majority (39) of these cores are concentrated in the central 1 pc area of the image.

### 3.2. Intensity distributions of molecular gas tracers

Figure 3 shows the velocity integrated intensity maps of the  $\text{H}^{13}\text{CO}^+$ ,  $\text{NH}_2\text{D}$  and  $\text{NH}_3$  emission, overlaid with the *Spitzer* 8  $\mu\text{m}$  emission. We detected significant  $\text{H}^{13}\text{CO}^+$  line emission coinciding with the 8  $\mu\text{m}$  dark filamentary structures, as well as with the majority of embedded dense cores. On the other hand, the  $\text{NH}_2\text{D}$  and  $\text{NH}_3$  line emissions are preferentially detected at the location of dense cores.

### 3.3. Line width and Mach number

#### 3.3.1. $\text{H}^{13}\text{CO}^+$

Single, double and triple velocity components were resolved in 84.8%, 15.1% and 1.1% of the areas where significant  $\text{H}^{13}\text{CO}^+$  emission was detected (Table 2). We refer to spectra with single, double and triple velocity components as  $v_1$ ,  $v_2$  and  $v_3$ , respectively. We found a  $\langle\sigma_{\text{obs}}\rangle = 0.31 \text{ km s}^{-1}$  mean observed velocity dispersion<sup>2</sup> from the dense cores, and a  $\langle\sigma_{\text{obs}}\rangle = 0.23 \text{ km s}^{-1}$  mean observed velocity dispersion exterior to the dense cores. The area of each dense core is marked with an open ellipse in Figure 1, while the remaining regions in the NGC 6334S are defined as areas exterior to the dense cores. The non-thermal velocity dispersion ( $\sigma_{\text{nt}}$ ) of the  $\text{H}^{13}\text{CO}^+$  line was estimated by

$$\sigma_{\text{nt}} = \sqrt{\left(\sigma_{\text{obs}}^2 - \Delta_{\text{ch}}^2 / (2\sqrt{2} \ln 2)^2\right) - \sigma_{\text{th}}^2}, \quad \text{where } \Delta_{\text{ch}} \text{ and } \sigma_{\text{th}} \text{ are velocity channel width and thermal velocity dispersion, respectively. The molecular thermal velocity dispersion was estimated by } \sigma_{\text{th}} = \sqrt{(k_{\text{B}}T)/(\mu m_{\text{H}})} = 9.08 \times 10^{-2} \text{ km s}^{-1} \left(\frac{T}{\text{K}}\right)^{0.5} \mu^{-0.5}, \text{ where } \mu = m/m_{\text{H}} \text{ is the molecular weight, } m \text{ is the molecular mass, } m_{\text{H}} \text{ is the proton mass, } k_{\text{B}} \text{ is the Boltzmann constant, and } T \text{ is the gas temperature. The thermal velocity dispersion (sound speed } c_{\text{s}}) \text{ of the particle of mean mass was estimated assuming a mean mass of gas of } 2.37 m_{\text{H}} \text{ (Kauffmann et al. 2008). The gas temperatures, } T_{\text{NH}_3}, \text{ derived from the } \text{NH}_3 \text{ line ratios were used to calculate the thermal velocity dispersion (Figure 2, see Section 2.3). We assumed a gas kinetic temperature of } \langle T_{\text{NH}_3} \rangle = 15 \text{ K for regions where the } \text{NH}_3 \text{ detection is insufficient for our temperature fittings or without } \text{NH}_3 \text{ observations. For each of the velocity components observed from the entire NGC 6334S region we also derived the Mach number, } \mathcal{M} = \sqrt{3}\sigma_{\text{nt}}/c_{\text{s}}. \text{ The derived Mach numbers range from 0.02 to 6.3, with a mean value of 1.5.}$$

Figure 4 shows the Mach number map of NGC 6334S. From this map, it appears that non-thermal motions in the majority of the observed regions are subsonic or transonic ( $0 < \mathcal{M} < 2$ ). The upper left panel of Figure 5 shows a normalized histogram of Mach numbers, which is derived from the regions in which is detected one single velocity component. We found that the  $\sigma_{\text{nt}}$  values of 29.6%, 46.4%, and 24% of these regions are subsonic ( $\mathcal{M} \leq 1$ ), transonic ( $1 < \mathcal{M} \leq 2$ ), and supersonic ( $\mathcal{M} > 2$ ), respectively (for a complete summary see Table 2).

The upper right panel of Figure 5 shows the histograms of Mach numbers derived from all observed velocity components. The contribution from the areas of dense cores and from the areas exterior to the dense cores are distinguished with colors. From areas exterior to the dense cores, we observed a histogram similar to the one presented in the left panel of Figure 5. We found systematically higher yet mostly still subsonic-to-transonic Mach numbers in the areas of dense cores. As can be seen from Figure 4, supersonic motions are mostly found in the central part of NGC 6334S, where there are multiple velocity components around dense cores. In summary, the non-thermal motions in the NGC 6334S cloud and the embedded dense cores are predominantly subsonic and transonic.

#### 3.3.2. $\text{NH}_2\text{D}$

In 89.3% and 10.7% of the regions with  $\text{NH}_2\text{D}$  emission, we resolved single and double velocity components, respectively. The mean  $\sigma_{\text{obs}}$  of the  $\text{NH}_2\text{D}$  line is  $0.21 \text{ km s}^{-1}$  and  $0.16 \text{ km s}^{-1}$  for the dense cores and the remaining region in NGC 6334S, respectively, which are smaller

<sup>2</sup> The one-dimensional observed velocity dispersion  $\sigma_{\text{obs}}$  is related to FWHM, define as  $\sigma_{\text{obs}} = \text{FWHM}/(2\sqrt{2} \ln 2)$ .

than those of the  $\text{H}^{13}\text{CO}^+$  line. Explanations for this discrepancy are discussed further in Section 4.2.2. The Mach numbers estimated from the  $\text{NH}_2\text{D}$  line range from 0.01 to 3.7, with a mean value of 1 (Table 2). The majority of cores (89%) have a mean Mach number of less than 2, and 43% of cores have a mean Mach number smaller than 1. Figure 5 shows the normalized histogram of Mach numbers estimated from the  $\text{NH}_2\text{D}$  line, which indicates that Mach numbers are smaller than 2 at the majority of regions, and are between 2 and 3 in 4.9% of the observed regions.

### 3.4. Dense Core Properties

With the observed 3 mm continuum fluxes, we estimated the gas mass ( $M_{\text{gas}}$ ) of identified cores assuming optically thin modified black body emission in the Rayleigh-Jeans limit, following

$$M_{\text{gas}} = \eta \frac{F_\nu d^2}{B_\nu(T) \kappa_\nu}, \quad (1)$$

where  $\eta = 100$  is the assumed gas-to-dust mass ratio,  $d$  is the source distance,  $F_\nu$  is the continuum flux at frequency  $\nu$ ,  $B_\nu(T)$  is the Planck function at temperature  $T$ , and  $\kappa_\nu$  is the dust opacity at frequency  $\nu$ . We adopt  $\kappa_{98.5 \text{ GHz}} = 0.235 \text{ cm}^2 \text{g}^{-1}$ , assuming  $\kappa_\nu = 10(\nu/1.2 \text{ THz})^\beta \text{ cm}^2 \text{g}^{-1}$  and  $\beta = 1.5$  for all of dense cores (Hildebrand 1983).

The derived gas masses are between 0.17 and  $14 M_\odot$ : two cores have masses of  $13 M_\odot$  and  $14 M_\odot$ ; the masses of 12 cores are between 2 and  $7 M_\odot$ ; the masses of the rest of the cores range from 0.17 to  $1.97 M_\odot$  (Table 1). Our  $1\sigma$  mass sensitivity corresponds to  $\sim 0.03 M_\odot$ . The uncertainty in the continuum flux is adopted to be a typical value of 10% in interferometer observations. The uncertainty in distance from the trigonometric parallax measurement is about 20% (Chibueze et al. 2014). The typical uncertainty in temperatures estimated from the  $\text{NH}_3$  lines is about 15%, which is mainly due to the low S/N in the  $\text{NH}_3$  data.  $\eta$  is adopted to be 100 in this study, while its standard deviation is 23 (corresponding to  $1\sigma$  uncertainty of 23%) assuming it is uniformly distributed between 70 and 150 (Devereux & Young 1990; Vuong et al. 2003; Sanhueza et al. 2017). We adopted a conservative uncertainty of 28% in  $\kappa_\nu$  (e.g., Sanhueza et al. 2017). Taking into account these uncertainties, we estimate an uncertainty of 57% for the gas mass.

Assuming spherical symmetry for identified dense cores, we evaluated their volume densities ( $n_{\text{H}_2} = M_{\text{gas}}/(\mu m_{\text{H}} 4\pi R^3/3)$ ) using the gas mass and effective radius. The derived volume densities vary between  $4.3 \times 10^5$  and  $2.2 \times 10^8 \text{ cm}^{-3}$ , with the mean and median value of  $1.1 \times 10^7$  and  $2.5 \times 10^6 \text{ cm}^{-3}$ , respectively. The

typical uncertainty is about 58% for volume density, with the exception of eight marginally resolved cores that have an uncertainty of  $> 100\%$  due to a large uncertainty in the beam-deconvolved effective radius.

For cores which were resolved with multiple velocity components (Appendix B), we further estimated the gas mass ( $M_i$ ) of each individual component  $i$  assuming that its continuum flux is  $F_{\text{cont}}^i = F_{\text{cont}}^{\text{tot}} \times I_{\text{line}}^i / I_{\text{line}}^{\text{tot}}$ , where  $F_{\text{cont}}^{\text{tot}}$  is the overall continuum flux,  $I_{\text{line}}^i$  is the velocity integrated intensity of the  $i$ th velocity component, and  $I_{\text{line}}^{\text{tot}} = \sum I_{\text{line}}^i$  is the overall velocity integrated intensity. This provides a reasonable estimate of gas mass for decomposed structures since the dense cores are dense enough ( $> 4 \times 10^5 \text{ cm}^{-3}$ ) for the gas and the dust to be well coupled (Goldsmith 2001). Using  $\text{H}^{13}\text{CO}^+$  emission, we have decomposed 67 structures (hereafter decomposed structures).

The virial ratio is evaluated for each decomposed structure using (Bertoldi & McKee 1992):

$$\alpha_{\text{vir}} = \frac{M_{\text{vir}}}{M_{\text{gas}}} \quad (2)$$

$$M_{\text{vir}} = \frac{5}{a\beta} \frac{\sigma_{\text{tot}}^2 R}{G}, \quad (3)$$

where  $M_{\text{vir}}$  is the virial mass,  $\sigma_{\text{tot}} = \sqrt{\sigma_{\text{int}}^2 + c_s^2}$  is the total velocity dispersion,  $R$  is the effective radius,  $G$  is the gravitational constant, parameter  $a$  equals to  $(1 - b/3)/(1 - 2b/5)$  for a power-law density profile  $\rho \propto r^{-b}$  (Bertoldi & McKee 1992), and  $\beta = (\arcsin e)/e$  is the geometry factor. Here, we assume a typical density profile of  $b = 1.6$  for all decomposed structures (Beuther et al. 2002; Butler & Tan 2012; Palau et al. 2014; Li et al. 2019a). The eccentricity  $e$  is determined by the axis ratio of the dense structure,  $e = \sqrt{1 - f_{\text{int}}^2}$ . The axis ratio of the decomposed structure is assumed to be the value of its corresponding dense core. Considering the projection effect and the dense cores are likely prolate ellipsoids (Myers et al. 1991), the observed axis ratio,  $f_{\text{obs}}$ , is larger than the intrinsic axis ratio,  $f_{\text{int}}$ . The  $f_{\text{int}}$  can be estimated from  $f_{\text{obs}}$  with

$$f_{\text{int}} = \frac{2}{\pi} f_{\text{obs}} \mathcal{F}_1(0.5, 0.5, -0.5, 1.5, 1, 1 - f_{\text{obs}}^2) \quad (4)$$

(Fall & Frenk 1983; Li et al. 2013), where  $\mathcal{F}_1$  is the Appell hypergeometric function of the first kind.

The corresponding virial mass of each velocity component is derived based on the corresponding effective radius,  $R_i = R \times \sqrt{A_i/A_{\text{core}}}$ . Here,  $R_i$  is the effective radius for the  $i$ th velocity component,  $R$  is the dense core beam-deconvolved effective radius (Table 1),  $A_i$  is the number of pixels for the  $i$ th velocity component within

the dense core measured in the moment-zeroth map, and the  $A_{\text{core}}$  is the number of pixels for the dense core (Figure 8).

Taking into account the uncertainties of  $\sigma_v$  and  $R$ , leads to an uncertainty of about 24% for virial mass. With the uncertainties of virial mass and dense core mass, the typical uncertainty is about 46% for the virial ratios, except for three marginal resolved dense cores that have an uncertainty of  $> 100\%$  due to the large uncertainty in the beam-deconvolved effective radius.

Based on the 67  $\text{H}^{13}\text{CO}^+$  decomposed structures, we found that the virial ratios range from 0.1 to 9.7, with the mean and median value of 1.8 and 1.4, respectively. Forty-three out of 67  $\text{H}^{13}\text{CO}^+$  decomposed structures have virial ratios smaller than 2, while 27 of them have ratios below 1. Non-magnetized cores with  $\alpha_{\text{vir}} < 2$ ,  $\alpha_{\text{vir}} \sim 1$  and  $\alpha_{\text{vir}} < 1$  are considered to be gravitationally bound, in hydrostatic equilibrium and gravitationally unstable, respectively (Bertoldi & McKee 1992; Kauffmann et al. 2013). Those with  $\alpha_{\text{vir}} > 2$  could be gravitationally unbound. Figure 6 shows the virial ratio versus the gas mass of the  $\text{H}^{13}\text{CO}^+$  decomposed structures. From this plot, it is apparent that there is an inverse relationship between the mass and the virial ratio. This indicates that the most massive structures tend to be more gravitationally unstable, while the less massive structures are gravitationally unbound and may eventually be disperse, unless there are other mechanism(s) that help to confine them such as external pressure and/or embedded protostar(s) with a significant mass.

We have decomposed 45 structures with the  $\text{NH}_2\text{D}$  emission. For these  $\text{NH}_2\text{D}$  decomposed structures, the derived virial ratios are between 0.1 and 12, with the mean and median values of 1.3 and 0.6, respectively. All of the  $\text{NH}_2\text{D}$  decomposed structures have virial ratios lower than 2, and 36 of them have ratios smaller than 1. This suggests that these decomposed structures are gravitationally bound. The analysis of both  $\text{NH}_2\text{D}$  and  $\text{H}^{13}\text{CO}^+$  give a similar result: the virial ratios of the decomposed structures decrease with increasing gas masses.

### 3.5. Pressure

Previous studies of star-forming regions have suggested that the external pressure provided by the ambient molecular cloud materials might help to confine dense structures in molecular clouds (Kirk et al. 2006; Liu et al. 2013a; Kirk et al. 2017; Seo et al. 2015; Pattle et al. 2015). In order to examine whether the external pressure can play a significant role in confining the dense structures, we estimate the external pressure from the

ambient cloud for each decomposed structure (McKee 1989; Kirk et al. 2017) using:

$$P_{\text{cl}} = \pi G \bar{\Sigma} \Sigma_r \beta_{\text{cl}}, \quad (5)$$

where  $P_{\text{cl}}$  is the gas pressure,  $\bar{\Sigma}$  is the mean column density of the cloud,  $\Sigma_r$  is the column density integrated from the cloud surface to depth  $r$ , and  $\beta_{\text{cl}}$  is the geometry factor for the cloud. We assumed that  $\Sigma_r$  is equal to half of the observed column density at the footprint of dense structures,  $\Sigma_r = \Sigma_{\text{obs}}/2$ , which is reasonable for most of star-forming regions (e.g., Kirk et al. 2006, 2017). To estimate the mean column density of a cloud, we consider only the central region where the mean column density of the cloud is about  $\bar{\Sigma} = 0.15 \text{ g cm}^{-2}$  estimated from the SED fitting (see Appendix A).

The derived external pressure of the  $\text{H}^{13}\text{CO}^+$  decomposed structures is between  $9.1 \times 10^6$  and  $1.9 \times 10^8 \text{ K cm}^{-3}$ , with a mean value of  $\langle P_{\text{cl}}/k_{\text{B}} \rangle = 3.8 \times 10^7 \text{ K cm}^{-3}$ . For the  $\text{NH}_2\text{D}$  decomposed structures, the derived external pressures range from  $9.1 \times 10^6$  to  $1.9 \times 10^8 \text{ K cm}^{-3}$ , with a mean value of  $\langle P_{\text{cl}}/k_{\text{B}} \rangle = 3.9 \times 10^7 \text{ K cm}^{-3}$ .

To determine the energy balance, we evaluated the external pressure energy, gravitational potential energy and internal kinetic energy in the virial equation (McKee 1989; Bertoldi & McKee 1992):

$$\Omega_P = -4\pi P_{\text{cl}} R^3 \quad (6)$$

$$\Omega_G = -\frac{3}{5} a \beta \frac{GM^2}{R} \quad (7)$$

$$\Omega_K = \frac{3}{2} M \sigma_{\text{tot}}^2 \quad (8)$$

where  $\Omega_P$ ,  $\Omega_G$  and  $\Omega_K$  are the external pressure, gravitational and kinetic terms, respectively.

For the  $\text{H}^{13}\text{CO}^+$  decomposed structure, the derived  $\Omega_P$  ranges from  $4.8 \times 10^{40}$  to  $4.1 \times 10^{44}$  erg, the  $\Omega_G$  is between  $3.7 \times 10^{40}$  and  $7.0 \times 10^{44}$  erg, and the  $\Omega_K$  is between  $3.7 \times 10^{40}$  and  $1.3 \times 10^{44}$  erg. The  $\text{NH}_2\text{D}$  decomposed structures have similar values compared to that of the  $\text{H}^{13}\text{CO}^+$  with the  $\Omega_P$  ranging from  $1.5 \times 10^{41}$  to  $4.1 \times 10^{44}$  erg, the  $\Omega_G$  between  $5.9 \times 10^{41}$  and  $7.9 \times 10^{44}$  erg, and the  $\Omega_K$  between  $5.2 \times 10^{41}$  and  $5.6 \times 10^{43}$  erg.

## 4. DISCUSSION

### 4.1. sonic-to-transonic motion

The mean observed values for  $\sigma_{\text{obs}}$  are about  $0.23 \text{ km s}^{-1}$  (or  $0.54 \text{ km s}^{-1}$  in FWHM) and  $0.17 \text{ km s}^{-1}$  (or  $0.40 \text{ km s}^{-1}$  in FWHM) for  $\text{H}^{13}\text{CO}^+$  and  $\text{NH}_2\text{D}$ , respectively, which indicates that the observed spectra are resolved in these ALMA observations with a spectral velocity channel width of  $0.21 \text{ km s}^{-1}$  (see also the Appendix C).

These line widths may be regarded as conservative upper limits, given the limited spectral resolution, the hyperfine line splittings, the blending of velocity components along the line-of-sight, and the outflows and shocks all of which can lead to overestimates of the line widths (Li et al. 2019b).

In spite of the aforementioned biases, from Figure 5 we can see that the spatially unresolved non-thermal motions are predominantly subsonic and transonic ( $\sim 77\%$  regions). The normalized distribution function of  $\mathcal{M}$  derived from the  $\text{H}^{13}\text{CO}^+$  observations peaks at 1.2. We have run a test with temperatures ranging from 8 to 25 K, corresponding to the range of the dust temperatures in the region, and found that 56% to up to 99% of Mach numbers are smaller than 2. This confirms that the Mach numbers are still dominated by subsonic and transonic motions within this temperature range.

More interestingly, such features persist down to the dense core scales ( $\sim 0.015$  pc) but with a higher fraction of larger Mach numbers as shown in Figure 5. There are several reasons that may cause the relatively broad line widths toward the dense cores. First, the line widths may be broadened by protostellar activities (e.g., outflow, infall, and/or rotation). Second, given that the majority of dense cores are associated with multiple velocity components, the line widths could be enhanced by the intersection of gas components at different velocities. Third, high optical depths could broaden the detected line widths (Hacar et al. 2016a). Unfortunately, we can not discriminate between these possibilities with the data at hand.

The subsonic-to-transonic dominated nature in both dense cores and NGC 6334S cloud suggests that these cores are still at very early evolutionary stages such that the protostellar feedback-induced turbulence is small as compared to the initial turbulence. Such low turbulence is similar to what is seen in low-mass star formation regions, e.g., Musca, L1517, NGC1333 and Taurus (Hacar & Tafalla 2011; Hacar et al. 2013, 2016b, 2017).

Figure 4 shows the spectral lines of the  $\text{H}^{13}\text{CO}^+$  at different spatial resolutions. It is clear that the line widths increase with increasing beam sizes. Therefore, the observed supersonic non-thermal velocity dispersions in massive star forming regions often reported in the literature might be significantly biased by the poor spatial resolution, since the spatially unresolved motions within the telescope beam can broaden the observed line widths.

#### 4.2. Dynamical State of Dense Cores

The relationship of decreasing  $\alpha_{\text{vir}}$  with  $M_{\text{gas}}$  shown in Figures 6 and 7 has also been reported in previous

studies of parsec scale massive clumps (Urquhart et al. 2015; Kauffmann et al. 2013), subparsec scale ( $\leq 0.1$  pc) massive dense cores (Li et al. 2019a), and low-mass star formation regions (Lada et al. 2008; Foster et al. 2009). Traficante et al. (2018) pointed out that such a decreasing trend of  $\alpha_{\text{vir}}$  may be attributed to systematic measurement errors when a particular molecular line preferentially traces molecular gas with densities above the critical density of the line transition. This effect could lead to a lower estimate of the virial parameter due to an underestimation of the observed line width. However, this effect may not be significant since the critical density of a given gas tracer is typically higher than the effective excitation density because of the effect of radiative trapping (Shirley 2015; Hull & Zhang 2019). The assumption of a certain density profile (equation 3, with  $b = 1.6$ ) could introduce some uncertainties to the virial mass, while it does not appear to be the dominant factor in the inverse  $\alpha_{\text{vir}} - M_{\text{gas}}$  relation since the density structures do not show significant differences between the massive cores and the low-mass cores (see for example, van der Tak et al. 2000; Motte & André 2001; Mueller et al. 2002; Shirley et al. 2002; Beuther et al. 2002; Butler & Tan 2012; Palau et al. 2014; Tobin et al. 2015; Li et al. 2019a).

Chemical segregation may introduce biases in the measurements of  $M_{\text{vir}}$ . For example, the study of the B-type star-forming region G192.16-3.84 (Liu et al. 2013b) found that the  $\text{H}^{13}\text{CO}^+$  emission did not trace the gravitationally accelerated, high-velocity gas that is probed by the  $\text{H}^{13}\text{CN}$  emission and other hot core tracers. The decreasing trend of  $\alpha_{\text{vir}}$  with  $M_{\text{gas}}$  therefore may be alternatively interpreted as indicating that higher mass cores evolve faster, and have lower  $\text{H}^{13}\text{CO}^+$  and  $\text{NH}_2\text{D}$  abundances at their centers. This hypothesis can be tested by spatially resolving gas temperature profiles for individual cores or by spatially resolving the abundance distribution of  $\text{H}^{13}\text{CO}^+$  and  $\text{NH}_2\text{D}$  at higher angular resolutions. Additionally, Vázquez-Semadeni et al. (2019) suggest that the core sample satisfies the relation  $M_{\text{gas}} \propto R^p$ , with  $0 < p < 3$ , would naturally yield an inverse  $\alpha_{\text{vir}} - M_{\text{gas}}$  relation.

On the other hand, investigations of a protocluster-forming molecular clump IRDC G28.34+0.06 have revealed that the line width decreases toward smaller spatial scales of denser regions (Wang et al. 2008). The change of line width could be due to dissipation of turbulence from the clump scale to core scale (Wang et al. 2008; Zhang et al. 2015). The spatially resolved studies of the OB cluster-forming molecular clump G33.92+0.11 (Liu et al. 2012, 2015, 2019) have demonstrated that in its inner  $\sim 0.5$  pc region, the turbulent energy is indeed

much less important as compared to the gravitational potential energy. Molecular gas in this region is highly gravitationally unstable, is collapsing towards the central ultra compact HII region, and is fragmenting to form a cluster of young stellar objects (YSOs). The 0.5 pc scale molecular clump and all embedded objects are detected with small  $M_{\text{vir}}$  and have  $\alpha_{\text{vir}} < 1$ , which is likely due to the fact that the dominant rotational and infall motions are perpendicular to the line-of-sight. Compared with our present observations on NGC 6334S, we hypothesize that turbulence in this case can dissipate more rapidly in cores with higher masses and higher densities. The diagnostics of the dynamical state of dense cores may require taking the projection effect into consideration; this can be tested by spatially resolving the gas motions within the identified cores.

#### 4.2.1. $\text{H}^{13}\text{CO}^+$ decomposed structures

Two observational biases can lead to an overestimate of the virial ratio: (1) overestimating the line width due to poor fitting; (2) incorrectly accounting for potential multiple velocity components not resolved in the current observations, which would broaden the observed line width. The observed velocity dispersions are similar among the identified cores with a mean value of  $0.31 \text{ km s}^{-1}$ , with the exception of one massive and one intermediate-mass cores having slightly larger observed velocity dispersion of around  $0.5 \text{ km s}^{-1}$ . To address the first issue, we inspected the line fitting of the  $\text{H}^{13}\text{CO}^+$  line for each core and removed or refitted the pixels with poor fitting in an effort to insure that the high virial ratio we measure in the less massive regimes is real. The second bias does not appear to be a significant factor in our dataset since the spectral resolution is high enough to resolve the observed lines (see the Appendix C). We conclude that the dense structures with high virial ratios are indeed unbound gravitationally.

The structures with high virial ratios may disperse and may not form stars in the future without additional mechanism(s) to counteract the internal pressures. In Section 3.4, our simplified virial analysis considered only balance between self-gravity and the internal support, and did not include the external pressure. In order to check whether the external pressure term plays an important role in confining the identified dense structures, we have computed the energy due to the external pressure ( $\Omega_P$ ), gravitational potential energy ( $\Omega_G$ ) and internal kinetic energy ( $\Omega_K$ ) (see Section 3.5).

When  $\Omega_P > \Omega_G$  the external pressure plays a dominant role in binding the dense structure, while  $\Omega_P < \Omega_G$  means that the gravity is the dominant element. In the panel c of Figure 6, we show the ratio of  $\Omega_G/\Omega_P$  ver-

sus the ratio of  $-(\Omega_G + \Omega_P)/2\Omega_K$ . The mean ratio of  $\Omega_G/\Omega_P$  is 8.9, with a median value of 1.4. From Figure 6, it is clear that the gravity dominates over the external pressure ( $\Omega_G/\Omega_P > 1$ ) for more than half (60%) of the structures, while 20 structures are dominated by the external pressure ( $\Omega_G/\Omega_P < 1$ ).

In the energy density form, the virial ratio is  $-2\Omega_K/(\Omega_G + \Omega_P)$ , when the external pressure is considered. In Figure 6, the vertical dashed line marks the locus of virial equilibrium. The structures that lie to the right of this line are confined by gravity and external pressure, while structures on the left of this line are unbound. The mean energy ratio of  $-(\Omega_G + \Omega_P)/2\Omega_K$  is about 3.6, with a median value of 1.8. As described in the previous paragraph (Section 3.4), a fraction (36%) of decomposed structures are gravitationally unbound in the simplified virial analysis, while most of them (79%) can be confined by gravity and external pressure,  $-(\Omega_G + \Omega_P)/2\Omega_K > 1$ . This suggests that the external pressure plays a role in confining the dense structures in this early evolutionary stage of star formation region. There are 14 structures which are not bound, even when accounting for the effect of external pressure.

In the above analysis, the external pressure only includes the pressure from the clump-scale cloud, but all of our dense cores are embedded within filamentary structures in the NGC 6334S cloud. These filaments could provide an additional external pressure on these dense cores. We are not able to accurately compute the filament pressure because it is difficult to extract the column density belonging to the filaments from this complex system. Kirk et al. (2017) suggests that the filament pressure is about a factor of 10 smaller than the pressure from the larger-scale cloud; however, this is a lower limit for their objects because they used parameters for low-mass star formation regions to estimate the filament pressure. The filament pressure in our sources could be higher than 10% of the pressure from the larger-scale cloud. In addition, the infall ram pressure is expected to provide an additional support to confine the dense cores (Heitsch et al. 2009; Kirk et al. 2017).

#### 4.2.2. $\text{NH}_2\text{D}$ decomposed structures

We also analyzed the energy density ratio for the  $\text{NH}_2\text{D}$  decomposed structures as shown in the panel d of Figure 7. These ratios behave in a similar way as in the  $\text{H}^{13}\text{CO}^+$  decomposed structures. The gravity plays a bigger role than the external pressure in confining 31 out of 45 structures with the other 14 structures being bound mostly due to the external pressure. In general, the virial ratio ( $\alpha_{\text{vir}}$  and  $-2\Omega_K/(\Omega_G + \Omega_P)$ ) of the  $\text{NH}_2\text{D}$  decomposed structures tends to be lower than those of



the  $\text{H}^{13}\text{CO}^+$ , due to the fact that the widths of the  $\text{NH}_2\text{D}$  line are narrower than those of the  $\text{H}^{13}\text{CO}^+$  line. The  $\text{NH}_2\text{D}$  emission traces colder gas and is less affected by the protostellar feedback (e.g., molecular outflows) as compared with the  $\text{H}^{13}\text{CO}^+$  emission. The derived line widths are also affected by the hyperfine splitting due to the limited spectral resolution. Overall, the results from both  $\text{NH}_2\text{D}$  and  $\text{H}^{13}\text{CO}^+$  lines are consistent, which supports our conclusion that the dense cores and their parent cloud are dominated by subsonic and transonic motions with external pressure helping to confine the younger and less massive dense structures.

## 5. CONCLUSION

We conducted ALMA and VLA observations toward the massive IRDC NGC 6334S. We used the cold and dense gas tracers,  $\text{H}^{13}\text{CO}^+$ ,  $\text{NH}_2\text{D}$  and  $\text{NH}_3$ , to study the gas properties from the clump scale down to the dense core scale. The main findings are

1. Forty-nine embedded dense cores are identified in the ALMA 3 mm dust continuum image. The majority of the cores are located in the central region of NGC 6334S and are embedded in filamentary structures. The masses of the dense cores range from 0.17 to  $14 M_\odot$ , with the effective radius between 0.005 and 0.041 pc.
2. The non-thermal velocity dispersion reveals that this massive cloud, as well as the embedded dense cores, are dominated by subsonic and transonic motions. The narrow non-thermal line widths resemble those seen in the low-mass star formation regions. Supersonic non-thermal velocity dispersions have been reported often in massive star forming regions. However, we caution that these studies might be significantly biased by poor spatial resolutions that broaden the observed line

widths due to unresolved motions within the telescope beam.

3. The majority of identified dense cores have multi-velocity components. We find that the virial ratios decrease with increasing mass despite the fact that they are dominated by subsonic and transonic motions. This implies that most massive structures tend to be gravitationally unstable. Most of dense structures can be confined by the gravity and external pressure, although a fraction of them are unbound. This result indicates that the external pressure plays a role in confining the dense structures during the early stages of star formation.

We thank an anonymous referee for constructive comments that help improving this paper. This work is supported by the National Key R&D Program of China (No. 2017YFA0402604) and the Natural Science Foundation of China under grant 11590783 and 11629302. S.L. acknowledges support from the CfA pre-doctoral fellowship and Chinese Scholarship Council. H.B. acknowledges support from the European Research Council under the Horizon 2020 Framework Program via the ERC Consolidator Grant CSF-648505. A.P. acknowledges financial support from CONACyT and UNAM-PAPIIT IN113119 grant, México. J.M.G. acknowledges support from MICINN AYA2017-84390-C3-2-R. ALMA is a partnership of ESO (representing its member states), NSF (USA) and NINS (Japan), together with NRC (Canada) and NSC and ASIAA (Taiwan), in cooperation with the Republic of Chile. The Joint ALMA Observatory is operated by ESO, AUI/NRAO and NAOJ.

*Facilities:* ALMA, JVLA, APEX, Planck, Herschel.

*Software:* APLpy (Robitaille & Bressert 2012), Astropy (Astropy Collaboration et al. 2013), CASA (McMullin et al. 2007), Matplotlib (Hunter 2007), Numpy (van der Walt et al. 2011), PySpecKit (Ginsburg & Mirocha 2011), SAOImageDS9 (Joye & Mandel 2003).

## REFERENCES

- Astropy Collaboration, Robitaille, T. P., Tollerud, E. J., et al. 2013, *A&A*, 558, A33
- Bergin, E. A., & Tafalla, M. 2007, *ARA&A*, 45, 339
- Bertoldi, F., & McKee, C. F. 1992, *ApJ*, 395, 140
- Beuther, H., Schilke, P., Menten, K. M., et al. 2002, *ApJ*, 566, 945
- Beuther, H., Soler, J. D., Vlemmings, W., et al. 2018, *A&A*, 614, A64
- Bonazzola, S., Heyvaerts, J., Falgarone, E., Perault, M., & Puget, J. L. 1987, *A&A*, 172, 293
- Busquet, G., Palau, A., Estalella, R., et al. 2010, *A&A*, 517, L6
- Butler, M. J., & Tan, J. C. 2012, *ApJ*, 754, 5
- Caselli, P., Benson, P. J., Myers, P. C., & Tafalla, M. 2002, *ApJ*, 572, 238
- Caselli, P., & Myers, P. C. 1995, *ApJ*, 446, 665

- Chibueze, J. O., Omodaka, T., Handa, T., et al. 2014, *ApJ*, 784, 114
- Daniel, F., Coudert, L. H., Punanova, A., et al. 2016, *A&A*, 586, L4
- Devereux, N. A., & Young, J. S. 1990, *ApJ*, 359, 42
- Elmegreen, B. G., & Scalo, J. 2004, *ARA&A*, 42, 211
- Fall, S. M., & Frenk, C. S. 1983, *AJ*, 88, 1626
- Foster, J. B., Rosolowsky, E. W., Kauffmann, J., et al. 2009, *ApJ*, 696, 298
- Friesen, R. K., Pineda, J. E., co-PIs, et al. 2017, *ApJ*, 843, 63
- Ginsburg, A., & Mirocha, J. 2011, *PySpecKit: Python Spectroscopic Toolkit*, *Astrophysics Source Code Library*, , ascl:1109.001
- Goldsmith, P. F. 2001, *ApJ*, 557, 736
- Goodman, A. A., Barranco, J. A., Wilner, D. J., & Heyer, M. H. 1998, *ApJ*, 504, 223
- Hacar, A., Alves, J., Burkert, A., & Goldsmith, P. 2016a, *A&A*, 591, A104
- Hacar, A., Kainulainen, J., Tafalla, M., Beuther, H., & Alves, J. 2016b, *A&A*, 587, A97
- Hacar, A., & Tafalla, M. 2011, *A&A*, 533, A34
- Hacar, A., Tafalla, M., & Alves, J. 2017, *A&A*, 606, A123
- Hacar, A., Tafalla, M., Forbrich, J., et al. 2018, *A&A*, 610, A77
- Hacar, A., Tafalla, M., Kauffmann, J., & Kovács, A. 2013, *A&A*, 554, A55
- Heitsch, F., Ballesteros-Paredes, J., & Hartmann, L. 2009, *ApJ*, 704, 1735
- Hennebelle, P., & Chabrier, G. 2008, *ApJ*, 684, 395
- Hildebrand, R. H. 1983, *QJRAS*, 24, 267
- Hull, C. L. H., & Zhang, Q. 2019, *Frontiers in Astronomy and Space Sciences*, 6, 3
- Hunter, J. D. 2007, *Computing In Science & Engineering*, 9, 90
- Joye, W. A., & Mandel, E. 2003, in *Astronomical Society of the Pacific Conference Series*, Vol. 295, *Astronomical Data Analysis Software and Systems XII*, ed. H. E. Payne, R. I. Jedrzejewski, & R. N. Hook, 489
- Kauffmann, J., Bertoldi, F., Bourke, T. L., Evans, N. J., I., & Lee, C. W. 2008, *A&A*, 487, 993
- Kauffmann, J., Pillai, T., & Goldsmith, P. F. 2013, *ApJ*, 779, 185
- Kirk, H., Johnstone, D., & Di Francesco, J. 2006, *ApJ*, 646, 1009
- Kirk, H., Friesen, R. K., Pineda, J. E., et al. 2017, *ApJ*, 846, 144
- Krumholz, M. R., & McKee, C. F. 2005, *ApJ*, 630, 250
- Lada, C. J., Muench, A. A., Rathborne, J., Alves, J. F., & Lombardi, M. 2008, *ApJ*, 672, 410
- Larson, R. B. 1981, *MNRAS*, 194, 809
- Li, D., Kauffmann, J., Zhang, Q., & Chen, W. 2013, *ApJL*, 768, L5
- Li, S., Zhang, Q., Pillai, T., et al. 2019a, *ApJ*, 886, 130
- Li, S., Wang, J., Zhang, Z.-Y., et al. 2017, *MNRAS*, 466, 248
- Li, S., Wang, J., Fang, M., et al. 2019b, *ApJ*, 878, 29
- Lin, Y., Liu, H. B., Li, D., et al. 2016, *The Astrophysical Journal*, 828, 32
- Lin, Y., Liu, H. B., Dale, J. E., et al. 2017, *The Astrophysical Journal*, 840, 22
- Liu, H. B., Galván-Madrid, R., Jiménez-Serra, I., et al. 2015, *ApJ*, 804, 37
- Liu, H. B., Ho, P. T. P., Wright, M. C. H., et al. 2013a, *ApJ*, 770, 44
- Liu, H. B., Jiménez-Serra, I., Ho, P. T. P., et al. 2012, *ApJ*, 756, 10
- Liu, H. B., Qiu, K., Zhang, Q., Girart, J. M., & Ho, P. T. P. 2013b, *ApJ*, 771, 71
- Liu, H. B., Chen, H.-R. V., Román-Zúñiga, C. G., et al. 2019, *ApJ*, 871, 185
- Mac Low, M.-M., & Klessen, R. S. 2004, *Reviews of Modern Physics*, 76, 125
- Mac Low, M.-M., Klessen, R. S., Burkert, A., & Smith, M. D. 1998, *Physical Review Letters*, 80, 2754
- McKee, C. F. 1989, *ApJ*, 345, 782
- McKee, C. F., & Ostriker, E. C. 2007, *ARA&A*, 45, 565
- McKee, C. F., & Tan, J. C. 2003, *ApJ*, 585, 850
- McMullin, J. P., Waters, B., Schiebel, D., Young, W., & Golap, K. 2007, in *Astronomical Society of the Pacific Conference Series*, Vol. 376, *Astronomical Data Analysis Software and Systems XVI*, ed. R. A. Shaw, F. Hill, & D. J. Bell, 127
- Monsch, K., Pineda, J. E., Liu, H. B., et al. 2018, *ApJ*, 861, 77
- Motte, F., & André, P. 2001, *A&A*, 365, 440
- Mueller, K. E., Shirley, Y. L., Evans, II, N. J., & Jacobson, H. R. 2002, *ApJS*, 143, 469
- Murray, N. 2011, *ApJ*, 729, 133
- Myers, P. C., Dame, T. M., Thaddeus, P., et al. 1986, *ApJ*, 301, 398
- Myers, P. C., Fuller, G. A., Goodman, A. A., & Benson, P. J. 1991, *ApJ*, 376, 561
- Myers, P. C., & Goodman, A. A. 1988, *ApJ*, 329, 392
- Palau, A., Estalella, R., Girart, J. M., et al. 2014, *ApJ*, 785, 42
- Pattle, K., Ward-Thompson, D., Kirk, J. M., et al. 2015, *MNRAS*, 450, 1094
- Persi, P., & Tapia, M. 2008, *Star Formation in NGC 6334*, ed. B. Reipurth, Vol. 5, 456

- Pillai, T., Kauffmann, J., Wyrowski, F., et al. 2011, *A&A*, 530, A118
- Pillai, T., Wyrowski, F., Hatchell, J., Gibb, A. G., & Thompson, M. A. 2007, *A&A*, 467, 207
- Pineda, J. E., Offner, S. S. R., Parker, R. J., et al. 2015, *Nature*, 518, 213
- Pirogov, L., Zinchenko, I., Caselli, P., Johansson, L. E. B., & Myers, P. C. 2003, *A&A*, 405, 639
- Robitaille, T., & Bressert, E. 2012, *APLpy: Astronomical Plotting Library in Python*, *Astrophysics Source Code Library*, , ascl:1208.017
- Russeau, D., Schneider, N., Anderson, L. D., et al. 2013, *A&A*, 554, A42
- Sanhueza, P., Jackson, J. M., Foster, J. B., et al. 2012, *ApJ*, 756, 60
- Sanhueza, P., Jackson, J. M., Zhang, Q., et al. 2017, *ApJ*, 841, 97
- Schmid-Burgk, J., Muders, D., Müller, H. S. P., & Brupbacher-Gatehouse, B. 2004, *A&A*, 419, 949
- Seo, Y. M., Shirley, Y. L., Goldsmith, P., et al. 2015, *ApJ*, 805, 185
- Shirley, Y. L. 2015, *PASP*, 127, 299
- Shirley, Y. L., Evans, Neal J., I., & Rawlings, J. M. C. 2002, *ApJ*, 575, 337
- Shirley, Y. L., Evans, II, N. J., Young, K. E., Knez, C., & Jaffe, D. T. 2003, *ApJS*, 149, 375
- Smith, R. J., Shetty, R., Beuther, H., Klessen, R. S., & Bonnell, I. A. 2013, *ApJ*, 771, 24
- Sokolov, V., Wang, K., Pineda, J. E., et al. 2018, *A&A*, 611, L3
- Stone, J. M., Ostriker, E. C., & Gammie, C. F. 1998, *ApJL*, 508, L99
- Tobin, J. J., Stutz, A. M., Megeath, S. T., et al. 2015, *ApJ*, 798, 128
- Traficante, A., Lee, Y.-N., Hennebelle, P., et al. 2018, *A&A*, 619, L7
- Urquhart, J. S., Figura, C. C., Moore, T. J. T., et al. 2015, *MNRAS*, 452, 4029
- van der Tak, F. F. S., van Dishoeck, E. F., Evans, II, N. J., & Blake, G. A. 2000, *ApJ*, 537, 283
- van der Walt, S., Colbert, S. C., & Varoquaux, G. 2011, *Computing in Science and Engineering*, 13, 22
- Vasyunina, T., Linz, H., Henning, T., et al. 2011, *A&A*, 527, A88
- Vázquez-Semadeni, E., Ostriker, E. C., Passot, T., Gammie, C. F., & Stone, J. M. 2000, in *Protostars and Planets IV*, ed. V. Mannings, A. P. Boss, & S. S. Russell, 3
- Vázquez-Semadeni, E., Palau, A., Ballesteros-Paredes, J., Gómez, G. C., & Zamora-Avilés, M. 2019, *MNRAS*, 490, 3061
- Vuong, M. H., Montmerle, T., Grosso, N., et al. 2003, *A&A*, 408, 581
- Vutisalchavakul, N., Evans, Neal J., I., & Heyer, M. 2016, *ApJ*, 831, 73
- Wang, Y., Zhang, Q., Pillai, T., Wyrowski, F., & Wu, Y. 2008, *ApJL*, 672, L33
- Willis, S., Marengo, M., Allen, L., et al. 2013, *ApJ*, 778, 96
- Zhang, Q., Wang, K., Lu, X., & Jiménez-Serra, I. 2015, *ApJ*, 804, 141

Table 1. Dense core properties

| Core ID | R.A.<br>(hh:mm:ss) | Decl.<br>(dd:mm:ss) | $\sigma_{maj}$<br>(arcsec) | $\sigma_{min}$<br>(arcsec) | PA<br>(deg) | $R_{\text{eff}}$<br>(arcsec) | $R_{\text{deff}}$<br>(arcsec) | $S_{\nu}^{\text{peak}}$<br>(mJy beam $^{-1}$ ) | $F_{\nu}$<br>(mJy) | $M_{\text{gas}}$<br>( $M_{\odot}$ ) | $T$<br>(K) | $\eta_{\text{H}_2}$<br>(cm $^{-3}$ ) |
|---------|--------------------|---------------------|----------------------------|----------------------------|-------------|------------------------------|-------------------------------|--|--------------------|-------------------------------------|------------|--------------------------------------|
| 1       | 17:19:07.41        | -36:07:14.16        | 13.51                      | 9.39                       | 124.46      | 6.76                         | 6.49                          | 1.213  | 1.846              | 14.03                               | 18         | 9.27E+05                             |
| 2       | 17:19:08.85        | -36:07:03.59        | 7.24                       | 4.53                       | 97.12       | 3.44                         | 2.93                          | 3.770  | 1.491              | 13.36                               | 15         | 9.72E+06                             |
| 3       | 17:19:05.92        | -36:07:21.43        | 6.55                       | 3.85                       | 77.05       | 3.02                         | 2.45                          | 2.771  | 0.837              | 6.93                                | 16         | 8.69E+06                             |
| 4       | 17:19:08.34        | -36:06:56.14        | 9.41                       | 5.85                       | 54.56       | 4.46                         | 4.06                          | 0.896  | 0.595              | 4.47                                | 18         | 1.23E+06                             |
| 5       | 17:19:09.39        | -36:06:31.18        | 5.17                       | 3.19                       | 79.69       | 2.44                         | 1.69                          | 2.896  | 0.574              | 5.19                                | 15         | 1.97E+07                             |
| 6       | 17:19:06.68        | -36:07:17.62        | 6.95                       | 6.51                       | 72.60       | 4.04                         | 3.61                          | 1.032  | 0.560              | 5.46                                | 14         | 2.14E+06                             |
| 7       | 17:19:05.23        | -36:07:50.55        | 3.98                       | 2.62                       | 81.06       | 1.94                         | 0.83                          | 3.749  | 0.467              | 6.67                                | 10         | 2.15E+08                             |
| 8       | 17:19:08.20        | -36:07:10.00        | 5.05                       | 3.13                       | 68.55       | 2.39                         | 1.58                          | 2.197  | 0.417              | 4.08                                | 14         | 1.92E+07                             |
| 9       | 17:19:08.36        | -36:04:31.70        | 5.16                       | 4.15                       | 67.48       | 2.78                         | 2.12                          | 1.134  | 0.307              | 2.77                                | 15         | 5.37E+06                             |
| 10      | 17:19:05.54        | -36:06:33.64        | 10.60                      | 7.49                       | 88.96       | 5.35                         | 5.05                          | 0.320  | 0.304              | 3.40                                | 13         | 4.84E+05                             |
| 11      | 17:19:06.03        | -36:07:16.98        | 4.96                       | 3.38                       | 80.35       | 2.46                         | 1.72                          | 1.343  | 0.270              | 1.80                                | 20         | 6.48E+06                             |
| 12      | 17:19:09.23        | -36:09:10.58        | 6.89                       | 5.21                       | 95.40       | 3.60                         | 3.12                          | 0.614  | 0.263              | 2.38                                | 15         | 1.44E+06                             |
| 13      | 17:19:12.92        | -36:06:13.95        | 8.99                       | 6.94                       | 160.36      | 4.74                         | 4.31                          | 0.334  | 0.252              | 2.28                                | 15         | 5.22E+05                             |
| 14      | 17:19:04.08        | -36:07:18.75        | 5.24                       | 4.17                       | 38.86       | 2.81                         | 2.05                          | 0.878  | 0.231              | 1.96                                | 16         | 4.15E+06                             |
| 15      | 17:18:59.99        | -36:07:19.56        | 4.43                       | 3.48                       | 78.65       | 2.36                         | 1.54                          | 0.927  | 0.229              | 2.61                                | 12         | 1.32E+07                             |
| 16      | 17:18:59.63        | -36:07:27.08        | 5.02                       | 3.22                       | 80.09       | 2.42                         | 1.66                          | 0.711  | 0.220              | 1.72                                | 17         | 6.90E+06                             |
| 17      | 17:19:09.27        | -36:06:24.85        | 6.76                       | 3.63                       | 91.57       | 2.98                         | 2.37                          | 0.737  | 0.218              | 1.97                                | 15         | 2.73E+06                             |
| 18      | 17:19:06.20        | -36:10:18.96        | 7.08                       | 5.25                       | 95.22       | 3.66                         | 3.20                          | 0.464  | 0.213              | 1.93                                | 15         | 1.08E+06                             |
| 19      | 17:19:06.04        | -36:07:11.91        | 9.76                       | 5.58                       | 88.28       | 4.43                         | 4.06                          | 0.287  | 0.188              | 1.48                                | 17         | 4.07E+05                             |
| 20      | 17:19:04.93        | -36:06:51.23        | 3.93                       | 3.45                       | 87.31       | 2.21                         | 1.17                          | 1.087  | 0.178              | 1.61                                | 15         | 1.83E+07                             |
| 21      | 17:19:05.93        | -36:10:24.93        | 7.68                       | 3.79                       | 84.00       | 3.24                         | 2.69                          | 0.459  | 0.172              | 1.56                                | 15         | 1.47E+06                             |
| 22      | 17:19:04.88        | -36:07:16.13        | 4.82                       | 3.05                       | 86.72       | 2.30                         | 1.48                          | 0.605  | 0.165              | 1.33                                | 16         | 7.56E+06                             |
| 23      | 17:19:11.91        | -36:07:01.46        | 4.82                       | 4.09                       | 25.94       | 2.67                         | 1.80                          | 0.929  | 0.165              | 1.49                                | 15         | 4.70E+06                             |
| 24      | 17:19:09.52        | -36:07:00.40        | 5.65                       | 5.61                       | 88.28       | 3.38                         | 2.82                          | 0.426  | 0.163              | 1.25                                | 17         | 1.02E+06                             |
| 25      | 17:19:06.43        | -36:10:29.03        | 6.21                       | 6.08                       | 178.28      | 3.69                         | 3.18                          | 0.315  | 0.156              | 1.41                                | 15         | 8.02E+05                             |
| 26      | 17:19:08.25        | -36:07:01.92        | 4.97                       | 3.57                       | 16.54       | 2.53                         | 1.09                          | 0.689  | 0.147              | 1.31                                | 15         | 1.87E+07                             |
| 27      | 17:19:09.13        | -36:06:36.59        | 5.84                       | 3.50                       | 88.28       | 2.71                         | 2.05                          | 0.467  | 0.115              | 1.86                                | 9          | 3.95E+06                             |
| 28      | 17:19:03.91        | -36:10:06.01        | 6.59                       | 4.57                       | 61.61       | 3.30                         | 2.76                          | 0.225  | 0.114              | 1.03                                | 15         | 9.01E+05                             |

Table 1 continued

Table 1 (continued)

| Core ID | R.A.<br>(hh:mm:ss) | Decl.<br>(dd:mm:ss) | $\sigma_{maj}$<br>(arcsec) | $\sigma_{min}$<br>(arcsec) | PA<br>(deg) | $R_{\text{eff}}$<br>(arcsec) | $R_{\text{deconv}}$<br>(arcsec) | $S_{\nu}^{\text{peak}}$<br>(mJy beam $^{-1}$ ) | $F_{\nu}$<br>(mJy) | $M_{\text{gas}}$<br>( $M_{\odot}$ ) | $T$<br>(K) | $n_{\text{H}_2}$<br>(cm $^{-3}$ ) |
|---------|--------------------|---------------------|----------------------------|----------------------------|-------------|------------------------------|---------------------------------|--|--------------------|-------------------------------------|------------|-----------------------------------|
| 29      | 17:19:12.42        | -36:08:58.99        | 8.43                       | 3.35                       | 122.53      | 3.19                         | 2.02                            | 0.234  | 0.111              | 1.00                                | 15         | 2.23E+06                          |
| 30      | 17:19:06.44        | -36:10:40.93        | 5.92                       | 4.58                       | 18.95       | 3.13                         | 2.40                            | 0.254  | 0.104              | 0.94                                | 15         | 1.25E+06                          |
| 31      | 17:19:04.90        | -36:07:55.00        | 5.47                       | 4.48                       | 103.28      | 2.98                         | 2.35                            | 0.311  | 0.092              | 2.54                                | 15         | 1.17E+06                          |
| 32      | 17:19:05.76        | -36:06:26.55        | 4.94                       | 4.30                       | 91.33       | 2.77                         | 2.09                            | 0.317  | 0.081              | 0.72                                | 15         | 1.46E+06                          |
| 33      | 17:19:05.87        | -36:05:38.76        | 3.99                       | 3.11                       | 95.33       | 2.12                         | 1.03                            | 0.417  | 0.080              | 0.72                                | 15         | 1.22E+07                          |
| 34      | 17:19:04.90        | -36:06:47.57        | 4.08                       | 2.31                       | 88.28       | 1.84                         | ...                             | 0.651  | 0.074              | 0.67                                | 15         | ...                               |
| 35      | 17:19:07.70        | -36:09:03.24        | 3.54                       | 2.38                       | 87.15       | 1.74                         | ...                             | 0.259  | 0.072              | 0.65                                | 15         | ...                               |
| 36      | 17:19:12.78        | -36:06:03.37        | 5.25                       | 4.42                       | 119.33      | 2.89                         | 2.20                            | 0.719  | 0.072              | 0.66                                | 15         | 1.14E+06                          |
| 37      | 17:19:05.13        | -36:07:44.19        | 6.42                       | 3.82                       | 79.90       | 2.97                         | 2.39                            | 0.236  | 0.069              | 0.89                                | 11         | 1.19E+06                          |
| 38      | 17:19:00.22        | -36:07:06.41        | 4.09                       | 3.53                       | 6.75        | 2.28                         | ...                             | 0.320  | 0.066              | 0.84                                | 11         | ...                               |
| 39      | 17:19:05.41        | -36:07:18.64        | 3.95                       | 2.90                       | 86.25       | 2.03                         | 0.97                            | 0.467  | 0.064              | 0.58                                | 15         | 1.18E+07                          |
| 40      | 17:19:09.35        | -36:06:51.91        | 4.62                       | 3.43                       | 101.73      | 2.39                         | 1.53                            | 0.331  | 0.063              | 0.49                                | 17         | 2.51E+06                          |
| 41      | 17:19:00.65        | -36:07:17.19        | 4.97                       | 3.68                       | 149.83      | 2.57                         | 1.26                            | 0.243  | 0.062              | 0.59                                | 14         | 5.40E+06                          |
| 42      | 17:19:06.47        | -36:06:25.96        | 5.71                       | 2.85                       | 88.60       | 2.42                         | 1.57                            | 0.284  | 0.056              | 0.53                                | 14         | 2.52E+06                          |
| 43      | 17:19:06.36        | -36:07:36.21        | 4.13                       | 3.00                       | 46.38       | 2.11                         | ...                             | 0.373  | 0.055              | 0.50                                | 15         | ...                               |
| 44      | 17:19:05.44        | -36:07:08.49        | 4.86                       | 2.92                       | 96.22       | 2.26                         | 1.32                            | 0.285  | 0.049              | 0.27                                | 23         | 2.18E+06                          |
| 45      | 17:19:03.99        | -36:07:01.38        | 4.37                       | 2.59                       | 79.76       | 2.02                         | 0.97                            | 0.313  | 0.043              | 0.39                                | 15         | 7.74E+06                          |
| 46      | 17:19:03.28        | -36:06:06.66        | 3.80                       | 2.98                       | 104.60      | 2.02                         | ...                             | 0.256  | 0.039              | 0.35                                | 15         | ...                               |
| 47      | 17:19:04.29        | -36:06:48.94        | 3.49                       | 2.99                       | 166.63      | 1.94                         | ...                             | 0.233  | 0.029              | 0.27                                | 15         | ...                               |
| 48      | 17:19:02.21        | -36:07:16.60        | 2.78                       | 2.25                       | 91.49       | 1.50                         | ...                             | 0.266  | 0.020              | 0.18                                | 15         | ...                               |
| 49      | 17:19:06.34        | -36:08:19.64        | 2.78                       | 2.38                       | 90.09       | 1.55                         | ...                             | 0.233  | 0.019              | 0.17                                | 15         | ...                               |

NOTE— R.A.: right ascension. Decl.: declination.  $\sigma_{maj}$ : beam-convolved major axis.  $\sigma_{min}$ : beam-convolved minor axis. PA: position angle.  $R_{\text{eff}}$ : beam-convolved effective radius.  $R_{\text{deconv}}$ : beam-deconvolved effective radius.  $F_{\nu}^{\text{peak}}$ : peak intensity.  $F_{\nu}$ : total integrated flux.  $M_{\text{gas}}$ : gas mass.  $T$ : temperature.  $n_{\text{H}_2}$ : averaged volume density.



**Table 2.** Mach number

| Line                       | Velocity component | Area | $\mathcal{M}$ | $\mathcal{M}_{\text{mean}}$ | $\mathcal{M}_{\text{median}}$ | $\mathcal{M} \leq 1$ | $1 < \mathcal{M} \leq 2$ | $\mathcal{M} > 2$ |
|----------------------------|--------------------|------|---------------|-----------------------------|-------------------------------|----------------------|--------------------------|-------------------|
| $\text{H}^{13}\text{CO}^+$ | $v_1$              | 0.72 | 0.02-6.3      | 1.5                         | 1.4                           | 29.6%                | 46.4%                    | 24%               |
|                            | $v_2$              | 0.13 | 0.04-5.4      | 1.5                         | 1.2                           | 32.9%                | 47.5%                    | 19.6%             |
|                            | $v_3$              | 0.01 | 0.1-5.1       | 1.4                         | 1.2                           | 32.5%                | 48.6%                    | 18.9%             |
|                            | All                | 0.86 | 0.02-6.3      | 1.5                         | 1.3                           | 30.1%                | 46.6%                    | 23.3%             |
| $\text{NH}_2\text{D}$      | $v_1$              | 0.25 | 0.01-3.7      | 1.0                         | 0.9                           | 57.8%                | 37.5%                    | 4.6%              |
|                            | $v_2$              | 0.03 | 0.05-3.0      | 1.0                         | 0.8                           | 61.2%                | 31.6%                    | 7.2%              |
|                            | All                | 0.28 | 0.01-3.7      | 1.0                         | 0.9                           | 58.2%                | 36.9%                    | 4.9%              |

NOTE— Area: the projection area in  $\text{pc}^2$ .  $v_1$ : single velocity component.  $v_2$ : double velocity components.  $v_3$ : triple velocity components. All: all emission components.

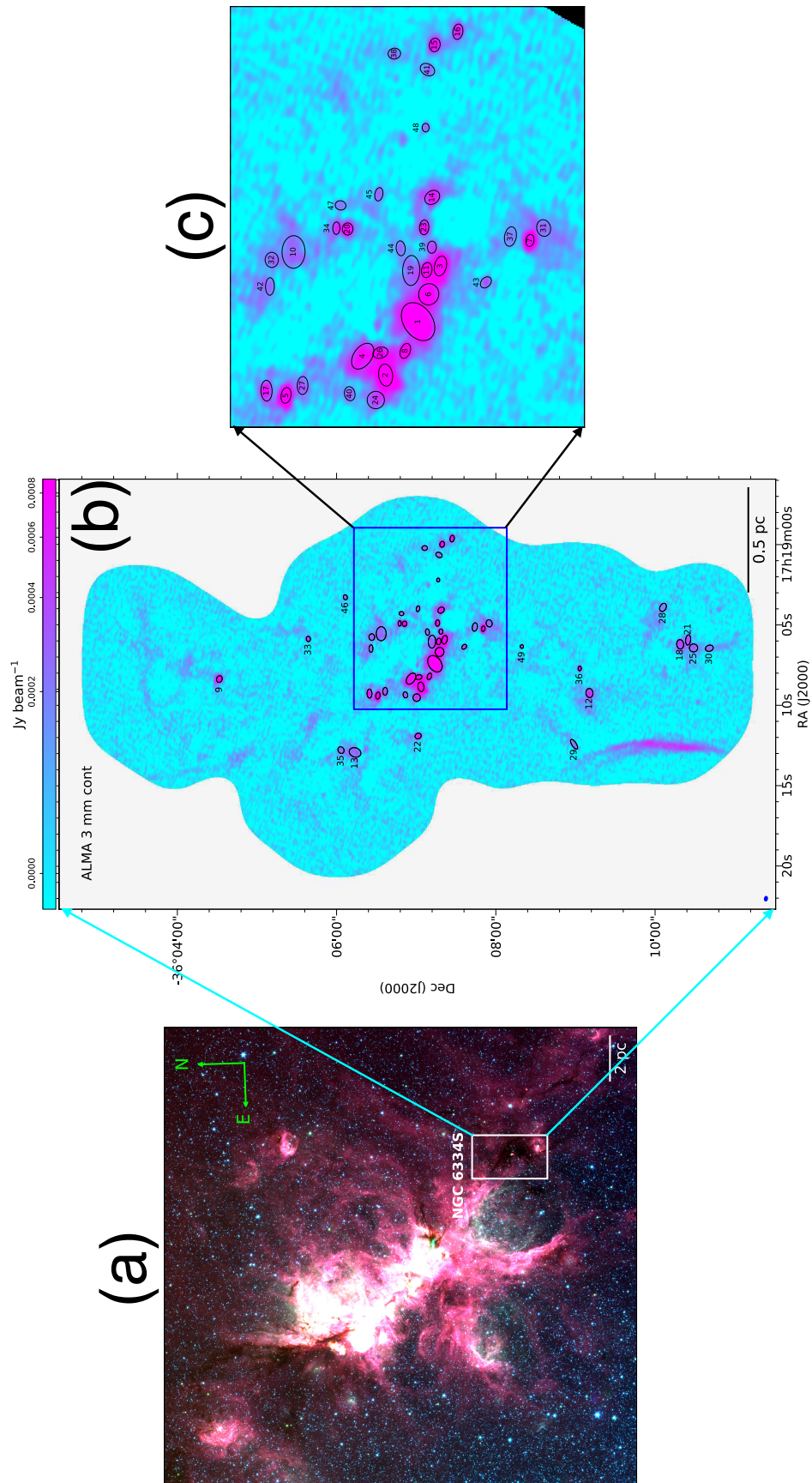


**Figure 1.** Panel a: three-color *Spitzer* composite image of the NGC 6334 molecular cloud complex with blue, green, and red representing data at  $\lambda = 3.6$ ,  $4.5$ , and  $8.0$   $\mu\text{m}$ , respectively. The image is centered at 17h20m02s, -35d54m03s. The scale bar is approximately 2 pc at the distance of 1.3 kpc. The white box presents the NGC 6334S region. Panel b: the ALMA 3 mm continuum image. The beam size is shown in the bottom left of the panel. Panel c: zoom in of the central region. The black ellipses present the identified dense cores.



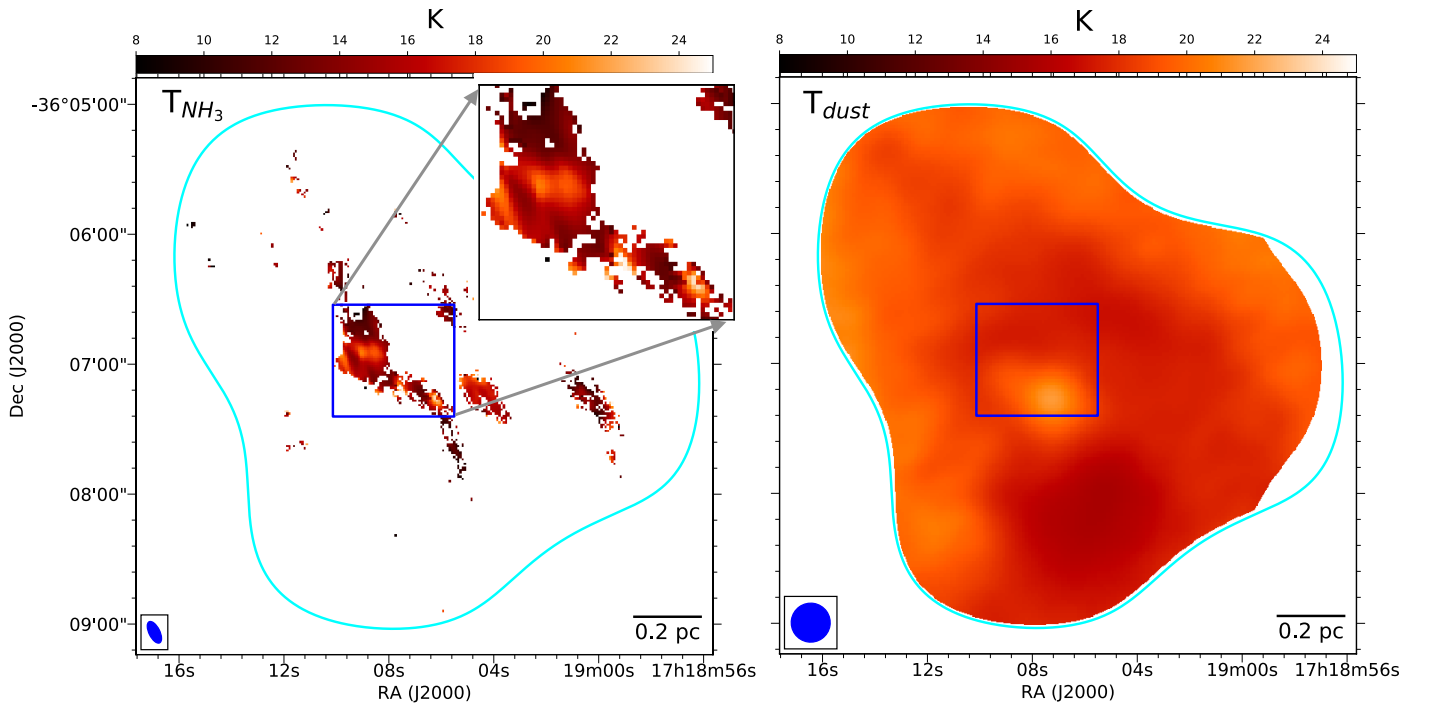


**Figure 2.** Left: temperatures derived from the  $NH_3$  data. The cyan line is the JVLA mosaic pattern. Right: the dust temperatures derived from SED fitting. The blue box marks the zooming in region in the left panel. The beam size is shown in the bottom left of the panel.

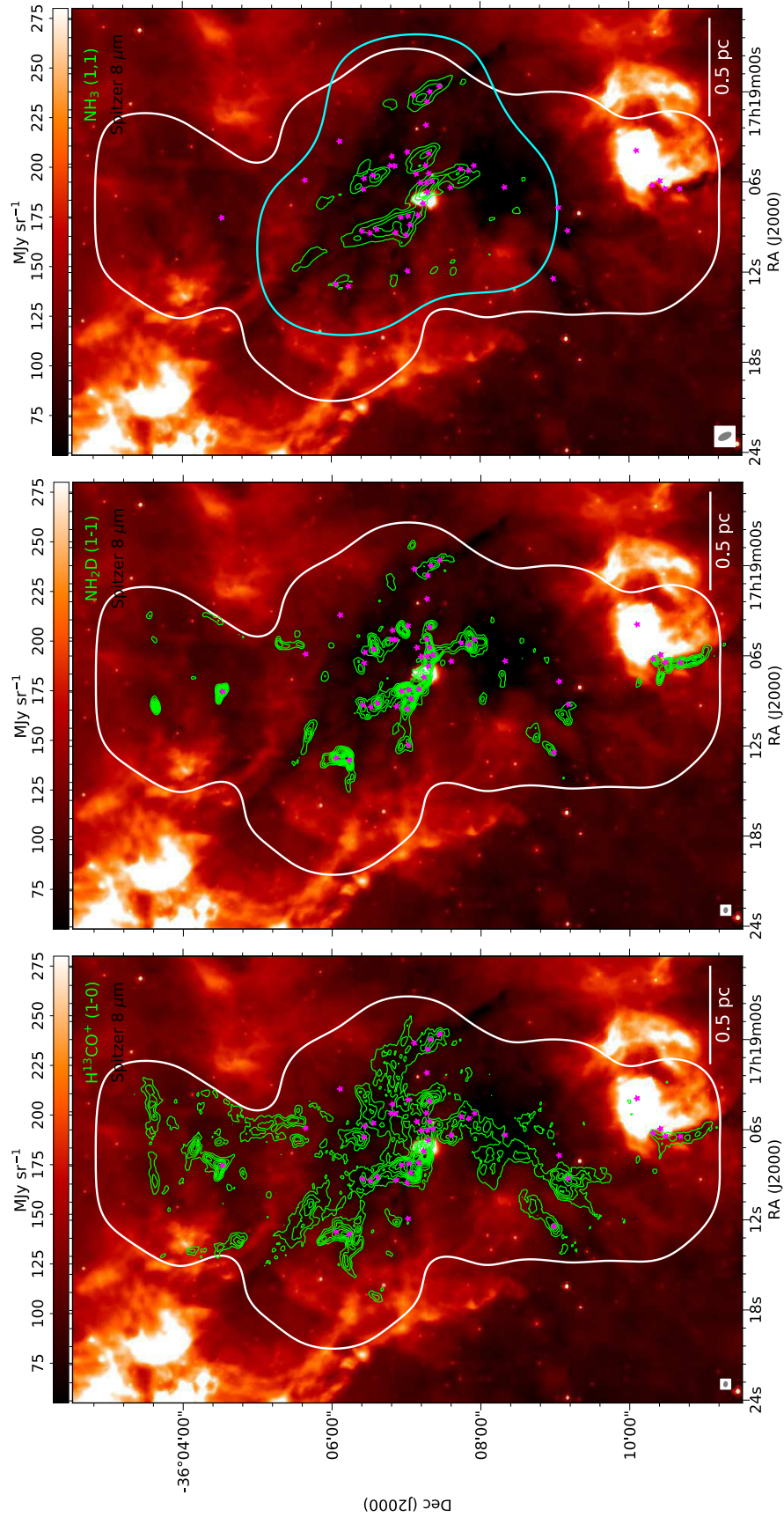


**Figure 3.** Figure shows the velocity integrated intensity map (green contours) of the  $\text{H}^{13}\text{CO}^+$  (1-0),  $\text{NH}_2\text{D}$  (1-1), and  $\text{NH}_3$  (1,1) overlaid on the Spitzer 8  $\mu\text{m}$  emission. The green contours are  $\pm(3, 6, 9 \dots) \times \sigma$ , where  $\sigma$  is the rms level for each line. The pink stars mark the dense cores revealed in the 3 mm continuum data. The white and cyan solid lines show the ALMA and VLA primary-beam responses at 20%, respectively. The beam size is shown in the bottom right of the panel.

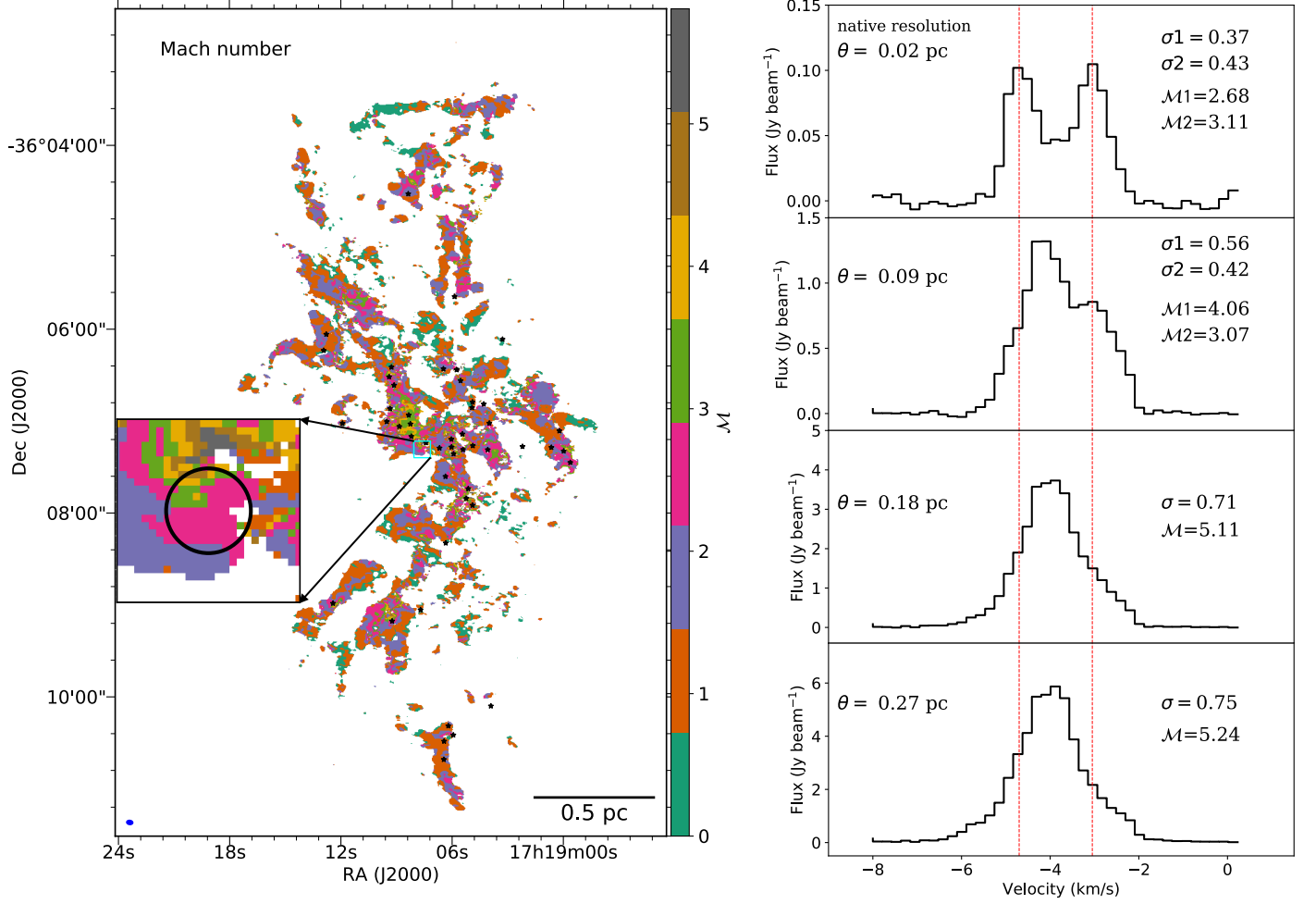


**Figure 4.** Left: Mach number map estimated from the  $\text{H}^{13}\text{CO}^+$  line for NGC 6334S. The black stars represent the identified dense cores. The beam size is shown in the bottom left of the panel. Right: averaged spectrum of the  $\text{H}^{13}\text{CO}^+$  line within the black circle showed on the left panel with different beam sizes. The two dashed vertical lines show the central velocities of the two velocity components measured at the native spatial resolution. The beam sizes ( $\theta$ ), velocity dispersion ( $\sigma_{\text{obs}}$ ) and Mach number are presented inside the panel.

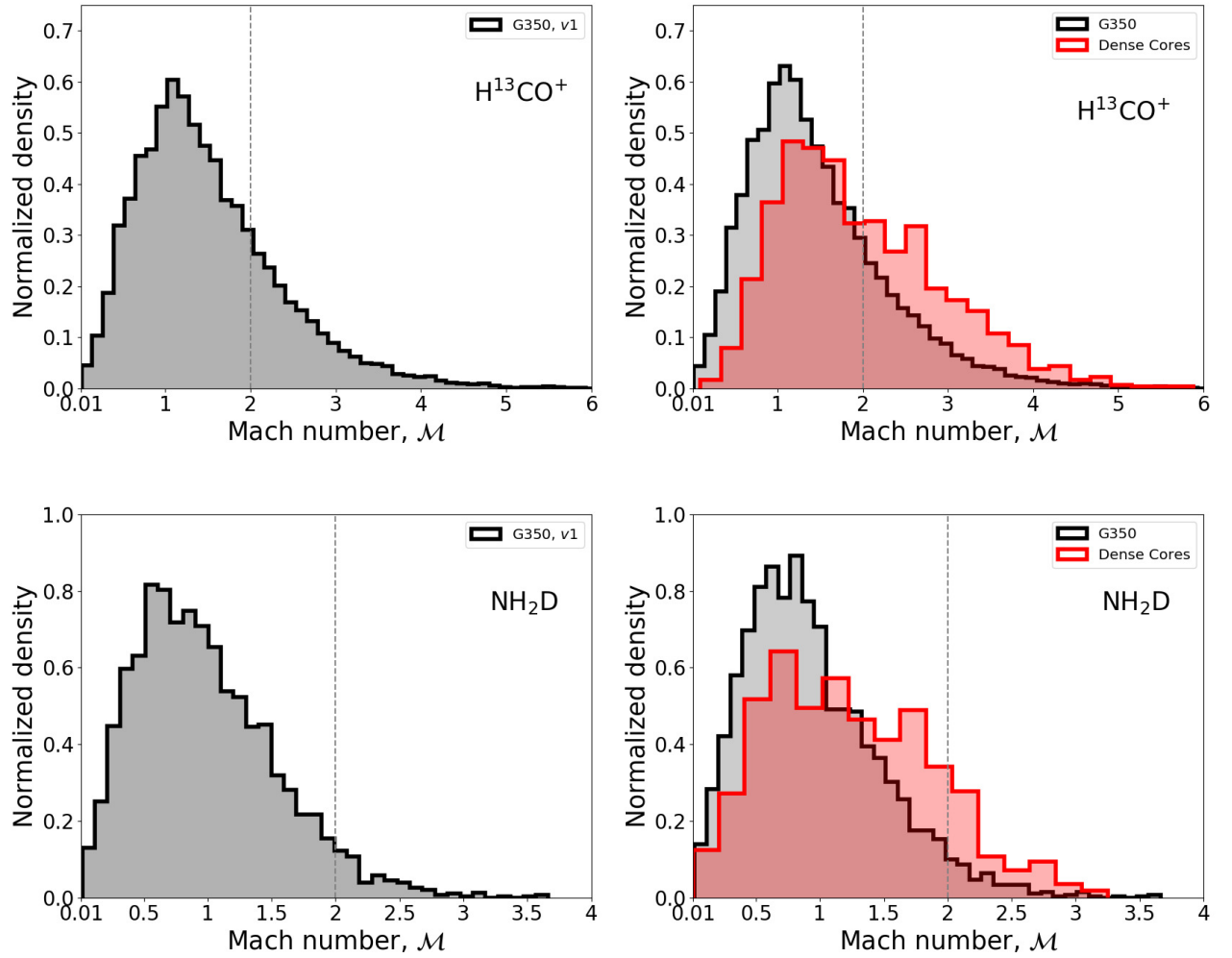


**Figure 5.** Gaussian kernel density estimate (KDE) of the Mach number distribution. Upper left: the distribution of Mach numbers for regions where a single velocity component was detected in NGC 6334S. Upper right: the distribution of Mach number for all velocity components for the entire NGC 6334S excluding the dense cores (black histogram), and for all velocity components from the dense cores only (red histogram). Bottom: same as the upper panels but using the  $\text{NH}_2\text{D}$  line. The grey vertical dash-dotted line represents the position of Mach number equal to 2.

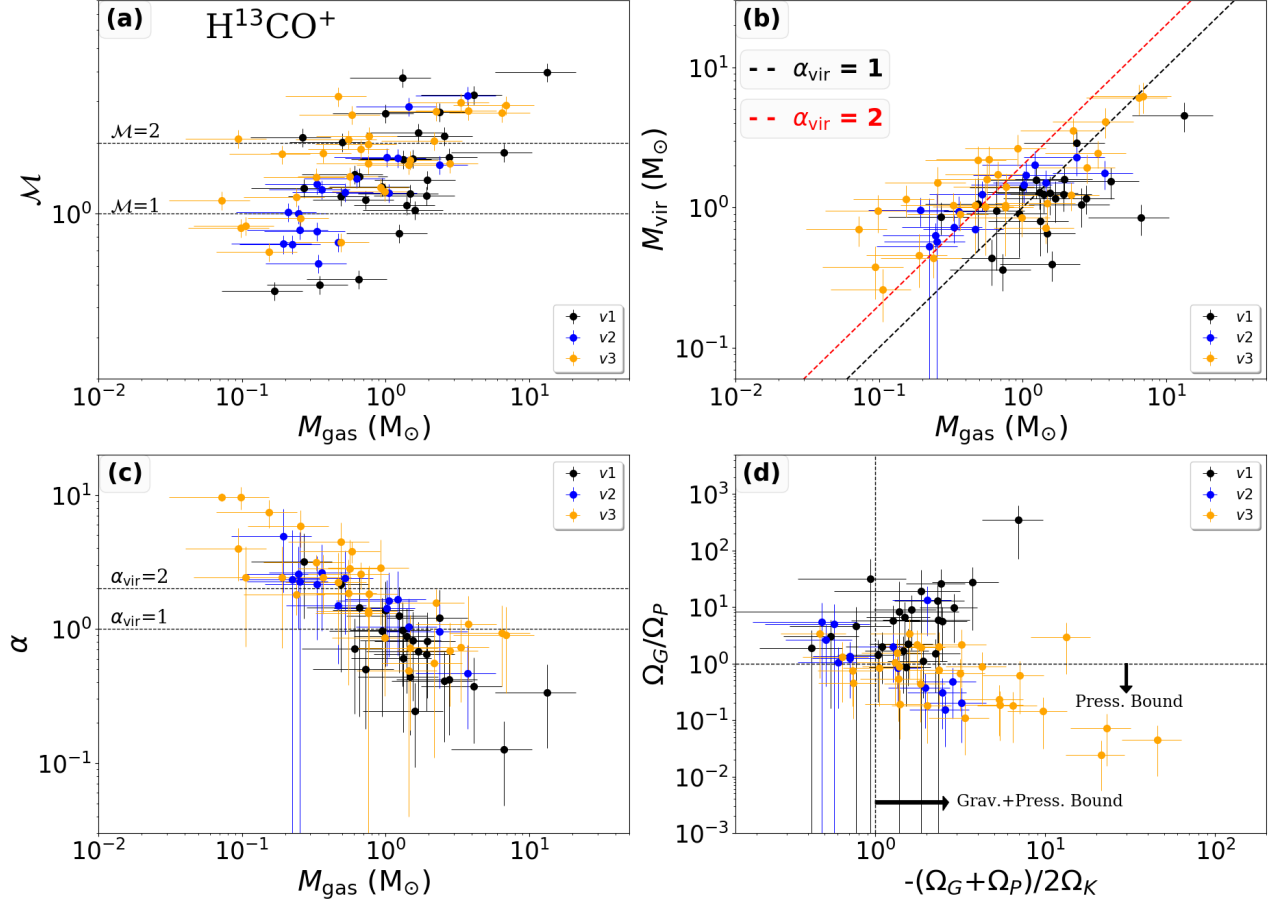


**Figure 6.** Panel a: Mach number versus gas mass for the  $\text{H}^{13}\text{CO}^+$  decomposed structures. Panel b: virial mass versus gas mass. The black and red dash-dotted lines show the  $\alpha_{\text{vir}} = 1$  and  $\alpha_{\text{vir}} = 2$  lines, respectively. Panel c: virial parameter versus gas mass. Panel d: the ratio of  $\Omega_G/\Omega_P$  versus ratio of  $-(\Omega_G + \Omega_P)/2\Omega_K$ .  $v1$ ,  $v2$  and  $v3$  represent the single, double and triple velocity components, respectively.

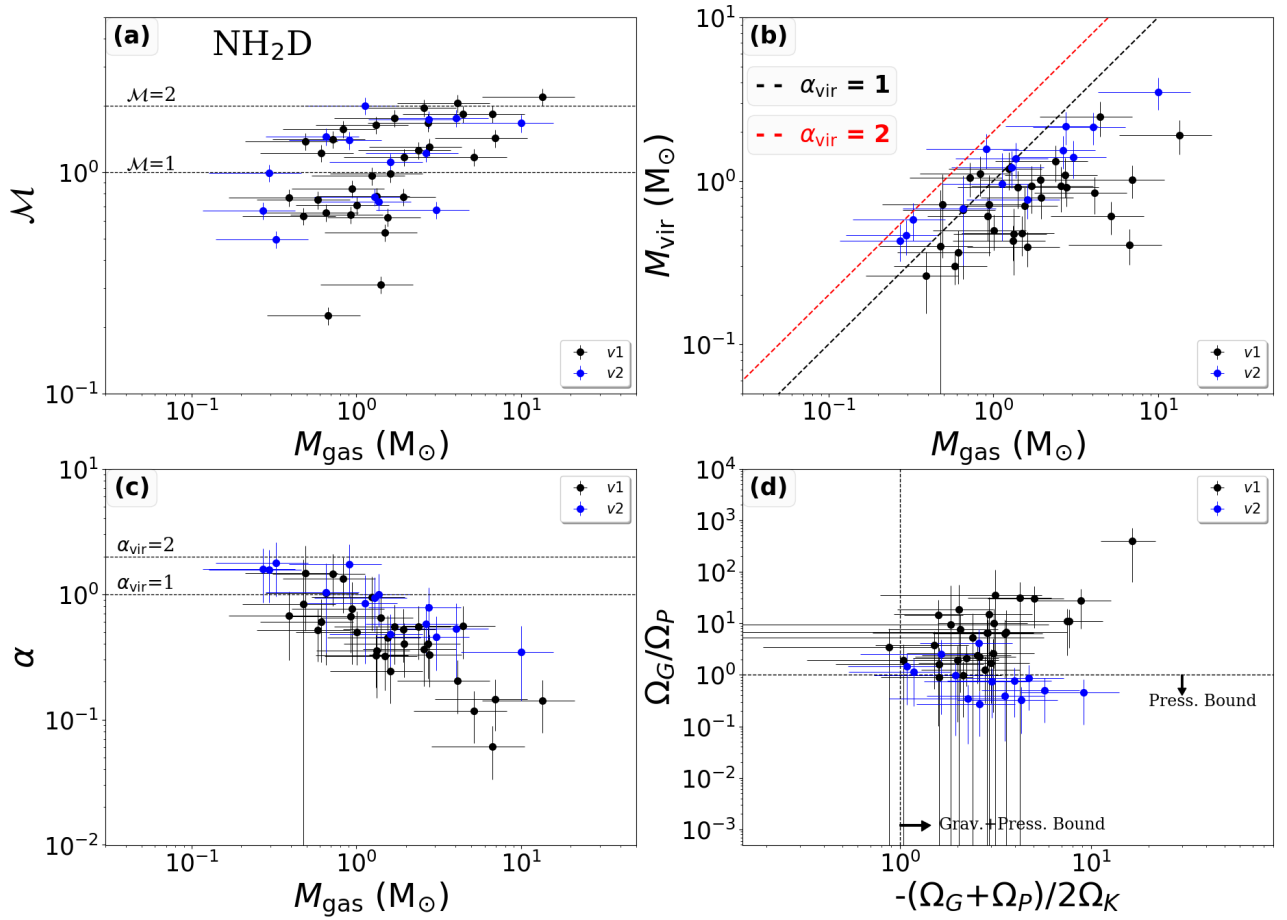


Figure 7. Same as Figure 6 but for the  $\text{NH}_2\text{D}$  decomposed structures.

## APPENDIX

## A. COLUMN DENSITY AND DUST TEMPERATURE

We adopted the image combination and SED fitting procedure presented in [Lin et al. \(2016, 2017\)](#). The procedure is briefly summarized here. **Planck** 353 GHz emission data are deconvolved using Lucy-Richardson algorithm with a model map from **Herschel** PACS 160  $\mu\text{m}$  (level2.5), SPIRE 250/350/500  $\mu\text{m}$  (level3) derived 870  $\mu\text{m}$  data. Then the deconvolved data were linearly combined with the ATLASGAL 870  $\mu\text{m}$  data in the Fourier domain. PACS 160  $\mu\text{m}$ , SPIRE 250  $\mu\text{m}$  and the combined 870  $\mu\text{m}$  data are used to fit the column density  $N(\text{H}_2)$  and dust temperature  $T_d$ , achieving a resolution of  $18''$ .

We performed an SED fit of each pixel, using a modified-black-body model:

$$I_\nu = B_\nu(T_d)(1 - e^{-\tau_\nu}) \quad (\text{A1})$$

where  $\tau_\nu = \mu m_{\text{H}} N(\text{H}_2) \kappa_\nu$ ,  $m_{\text{H}}$  is the mean molecular weight and we adopt a value of 2.8. We adopted a dust opacity law of  $\kappa_\nu = 10(\nu/1.2 \text{ THz})^\beta \text{ cm}^2\text{g}^{-1}$ , where  $\kappa_{353\text{GHz}} = 1.6$  is the dust opacity per unit mass (gas and dust) at reference frequency 353 GHz and  $\beta$  is fixed to 1.5 ([Hildebrand 1983](#)).

## B. DECOMPOSED STRUCTURES

As mentioned in Section 3.4, a dense core identified in dust continuum emission can be decomposed into sub-structures using the  $\text{H}^{13}\text{CO}^+$  and  $\text{NH}_2\text{D}$  lines. Figure 8 shows the spatial distributions of the decomposed structures and their spectral line profile. The estimations of gas mass and effective radius of the decomposed structures are described in Section 3.4.

The majority of decomposed structures identified using the  $\text{H}^{13}\text{CO}^+$  and  $\text{NH}_2\text{D}$  lines have similar gas masses and have significant overlap in projection (Figures 8 and 9), which indicates that they are consistent with each other. Some of the  $\text{H}^{13}\text{CO}^+$  and  $\text{NH}_2\text{D}$  decomposed structures partly overlap in projection; this is due to the discrepancy in the emission regions of the  $\text{H}^{13}\text{CO}^+$  and  $\text{NH}_2\text{D}$  lines, especially where the lines present multiple velocity components. This discrepancy is probably due to the presence of faint velocity components that are limited by the sensitivity of our observations. On the other hand, the  $\text{H}^{13}\text{CO}^+$  and  $\text{NH}_2\text{D}$  may trace slightly different gas components toward some dense cores, since they have different excitation conditions and chemical properties.

The detected multiple velocity components in a line profile could be attributed to optical depth effects, outflows, or a number of dense cores along the line of sight ([Smith et al. 2013](#)). Optical depth effects should not be the dominant mechanism causing the multiple velocity components in the line profile, since both  $\text{H}^{13}\text{CO}^+$  and  $\text{NH}_2\text{D}$  emission are generally optically thin, although these lines might become optically thick in the densest regions of the dense core. The narrow line widths seen in both  $\text{H}^{13}\text{CO}^+$  and  $\text{NH}_2\text{D}$  lines suggest that they are tracing quiescent rather than the shocked material. Therefore, the detected multiple velocity components in both  $\text{H}^{13}\text{CO}^+$  and  $\text{NH}_2\text{D}$  lines are most likely due to a number of dense cores along the line of sight (e.g., [Smith et al. 2013](#)).

## C. SIMULATION

To examine whether the observed line widths are biased by the spectral resolution or not, we constructed a simplified model. Assuming that the dense cores are in virial equilibrium ( $\alpha_{\text{vir}} = 1$ ), the virial velocity dispersion ( $\sigma_{\text{vir}}$ ) can be described by

$$\sigma_{\text{vir}} = \sqrt{\frac{\alpha_{\text{vir}} M_{\text{gas}} G}{5R}} \quad (\text{C2})$$

where  $M_{\text{gas}}$  and  $R$  are the gas mass and effective radius. We used the observed line intensity and  $\sigma_{\text{vir}}$  as input parameters to synthesize a spectrum with a spectral resolution of  $0.013 \text{ km s}^{-1}$  for dense cores (black lines in Figure 10). We fit Gaussian line profiles to the synthetic spectra, that have been smoothed to a spectral resolution of  $0.21 \text{ km s}^{-1}$  and with injected a random noise in 1000 iterations; we only show the dense cores that exhibit a single velocity component in the  $\text{H}^{13}\text{CO}^+$  emission. Figure 10 shows the fitting results. The fitted line width agrees with the input line width, indicating that the measured line widths are not significantly affected by the current spectral resolution in this study. We ran the same test for the  $\text{NH}_2\text{D}$  line, and reached the same conclusion.

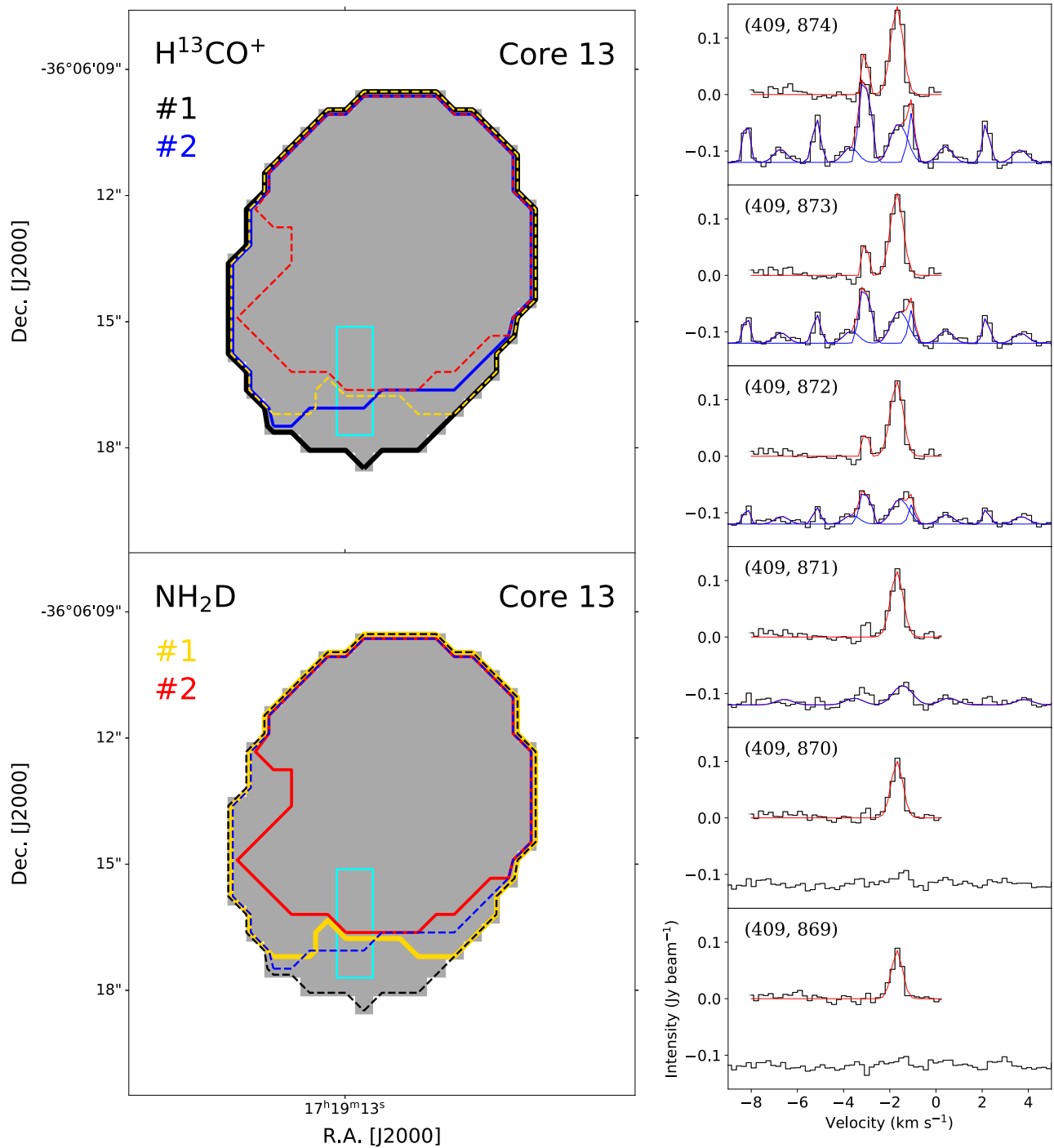


**Figure 8.** Left: schematic view of decomposed structures identified using the  $H^{13}CO^+$  (upper left) and  $NH_2D$  (bottom left) lines for dense core 13. The greyscale is the dense core revealed by the continuum emission. The black and blue contours represent the spatial distributions of the  $H^{13}CO^+$  decomposed structures, while the yellow and red contours represent the spatial distributions of the  $NH_2D$  decomposed structures. The contours are derived by the emission regions of corresponding velocity components, while #1 and #2 represent the first and second velocity components, respectively. Right: spectra of the  $H^{13}CO^+$  (upper) and  $NH_2D$  (lower) lines within the cyan rectangle shown on the left panel. For the  $H^{13}CO^+$  spectrum, the solid red curve represents the fitted result. For the  $NH_2D$  spectrum, the solid blue curve represents the components that are fitted, while solid red curve is the sum of them. The complete figure set (15 images) is available in the online journal.



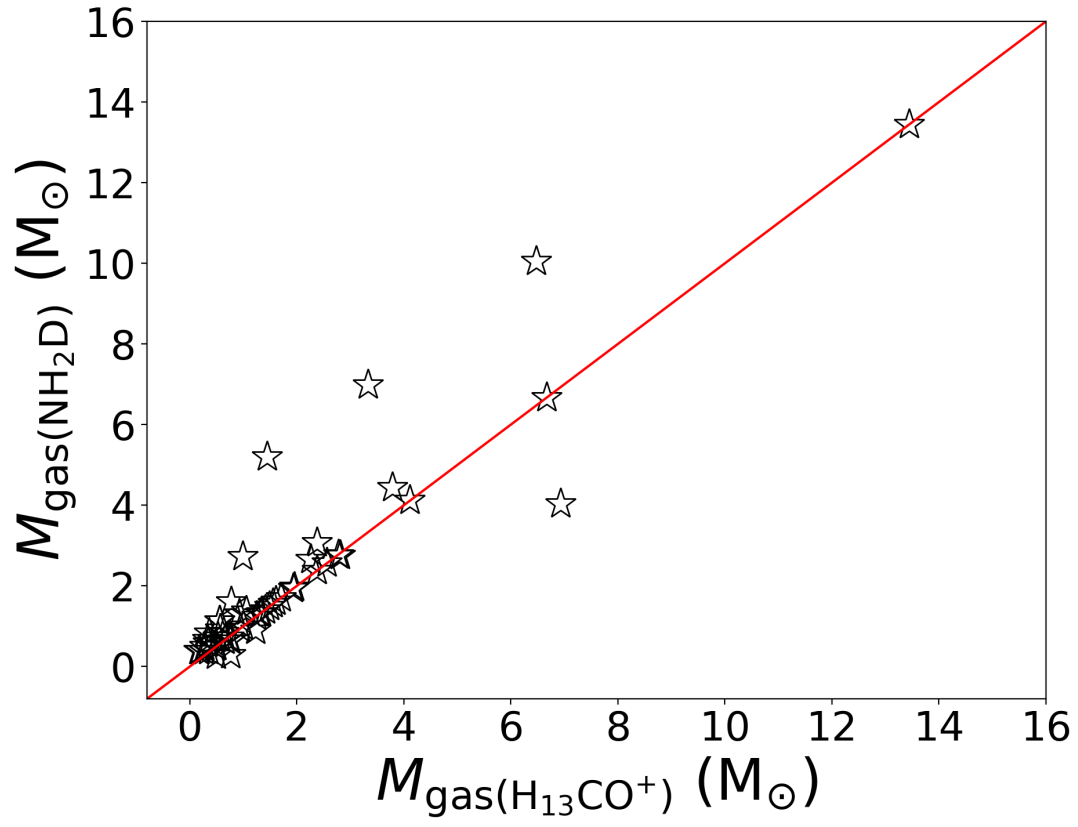


**Figure 9.** The gas masses of the  $\text{H}_{13}\text{CO}^+$  decomposed structures versus that of the  $\text{NH}_2\text{D}$  decomposed structures. The solid red line is the  $y = x$  line.

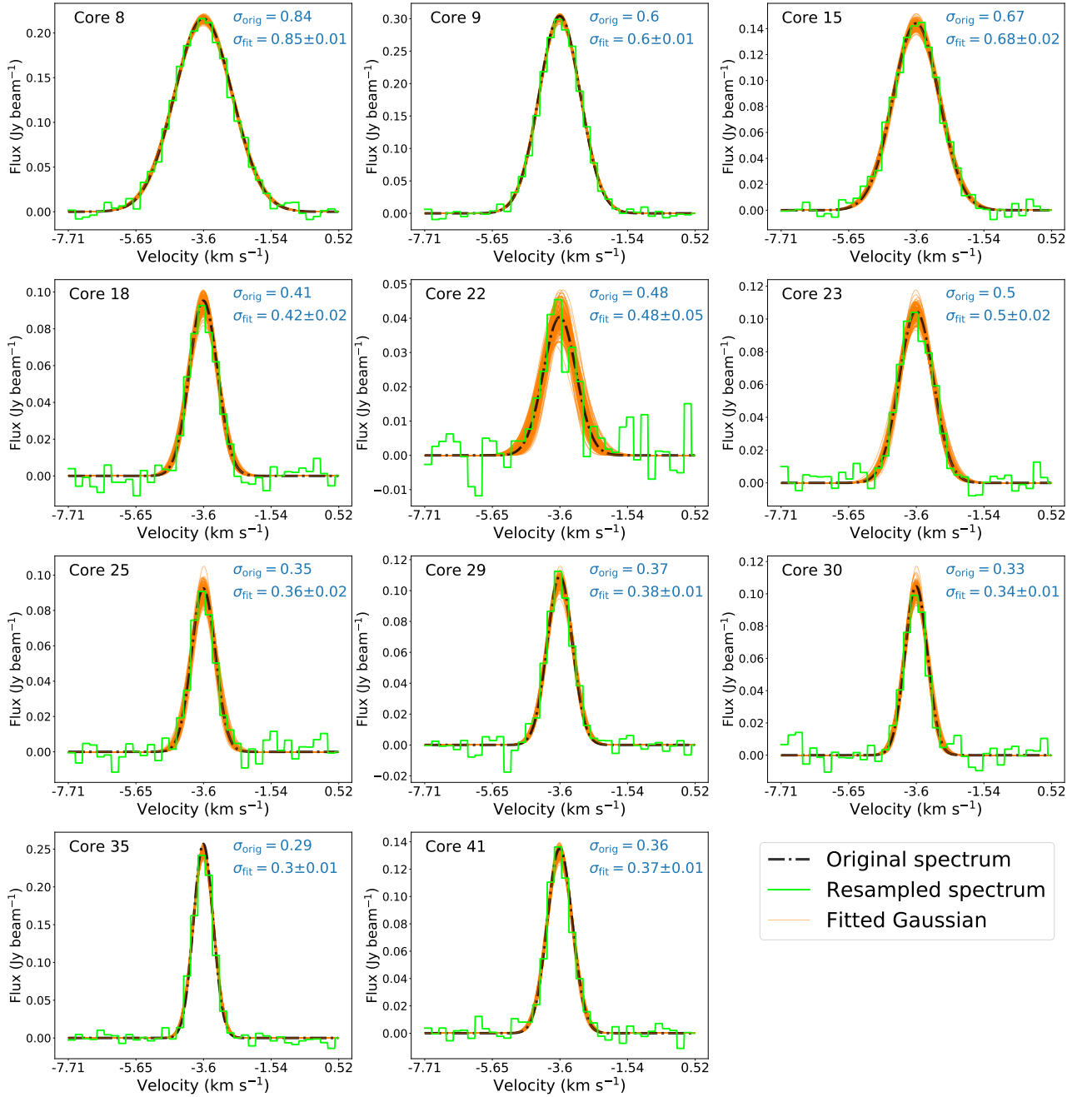
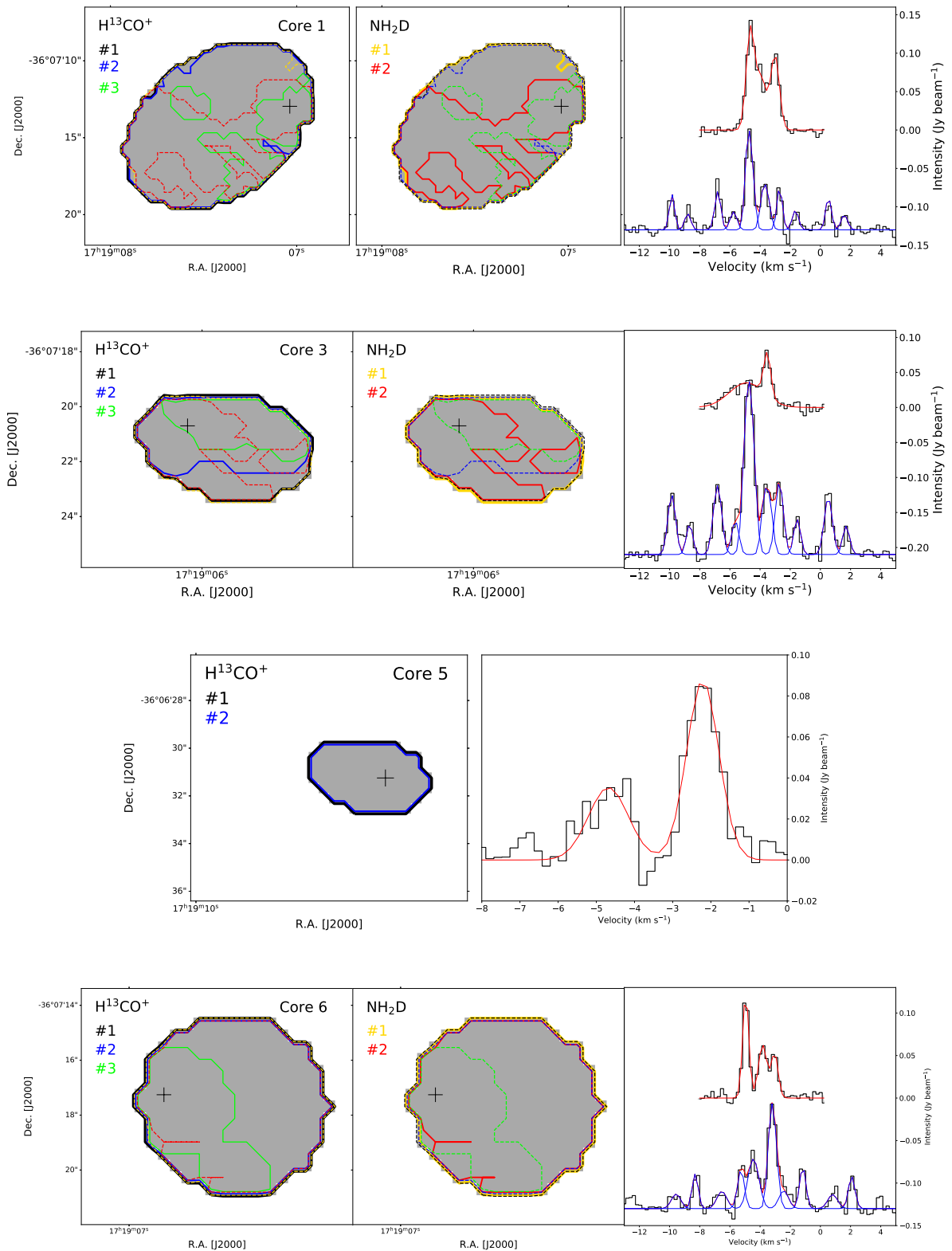
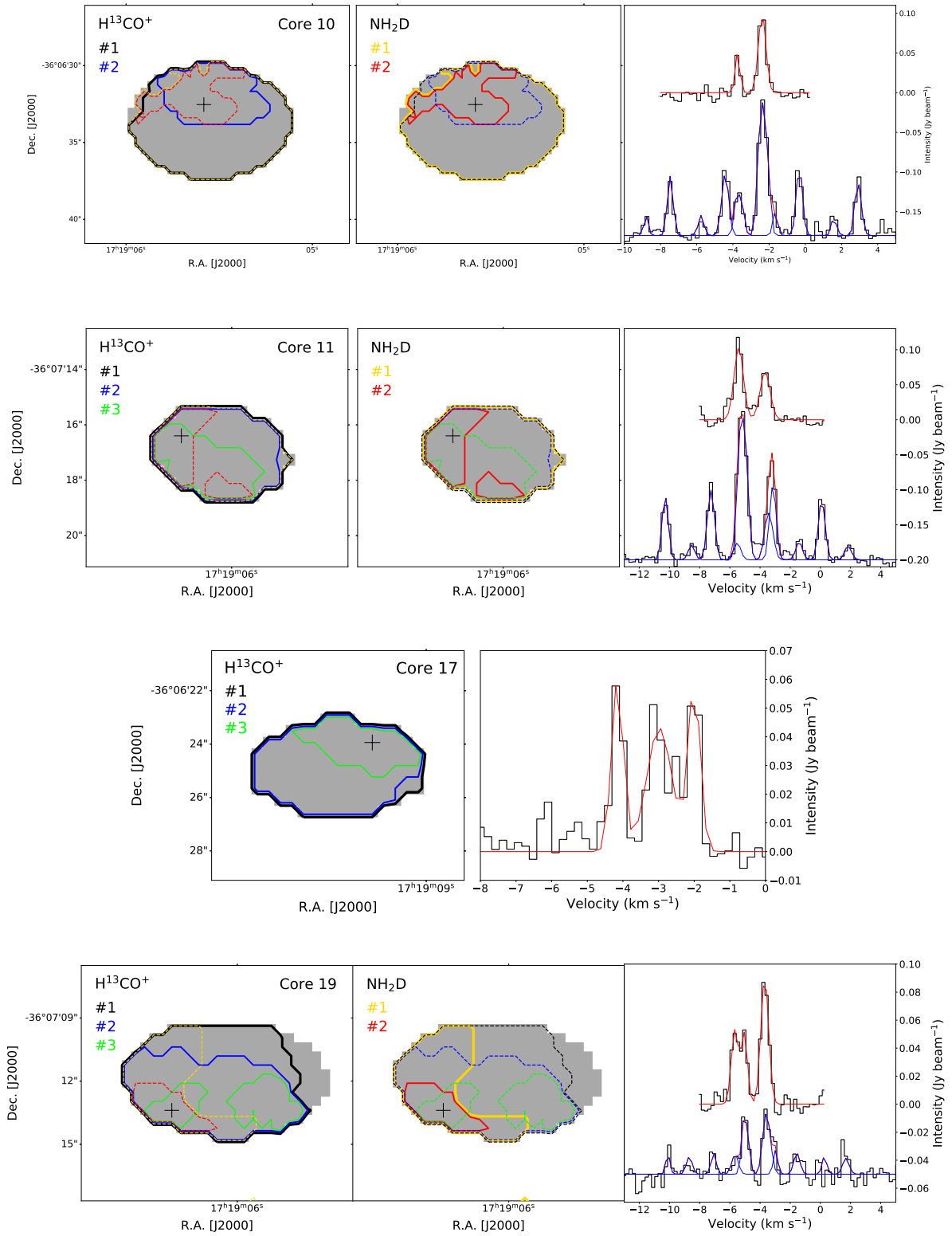


**Figure 10.** The black line is the original synthesized spectrum in the spectral resolution of 0.013 km s<sup>-1</sup>, while the green line is the original synthesized spectrum smoothed to a spectral resolution of 0.21 km s<sup>-1</sup>. The yellow lines are fitted results for each iteration. The dense core ID is presented on the upper left panel. The synthesized spectral line width and fitted line width are presented on the upper right panel.

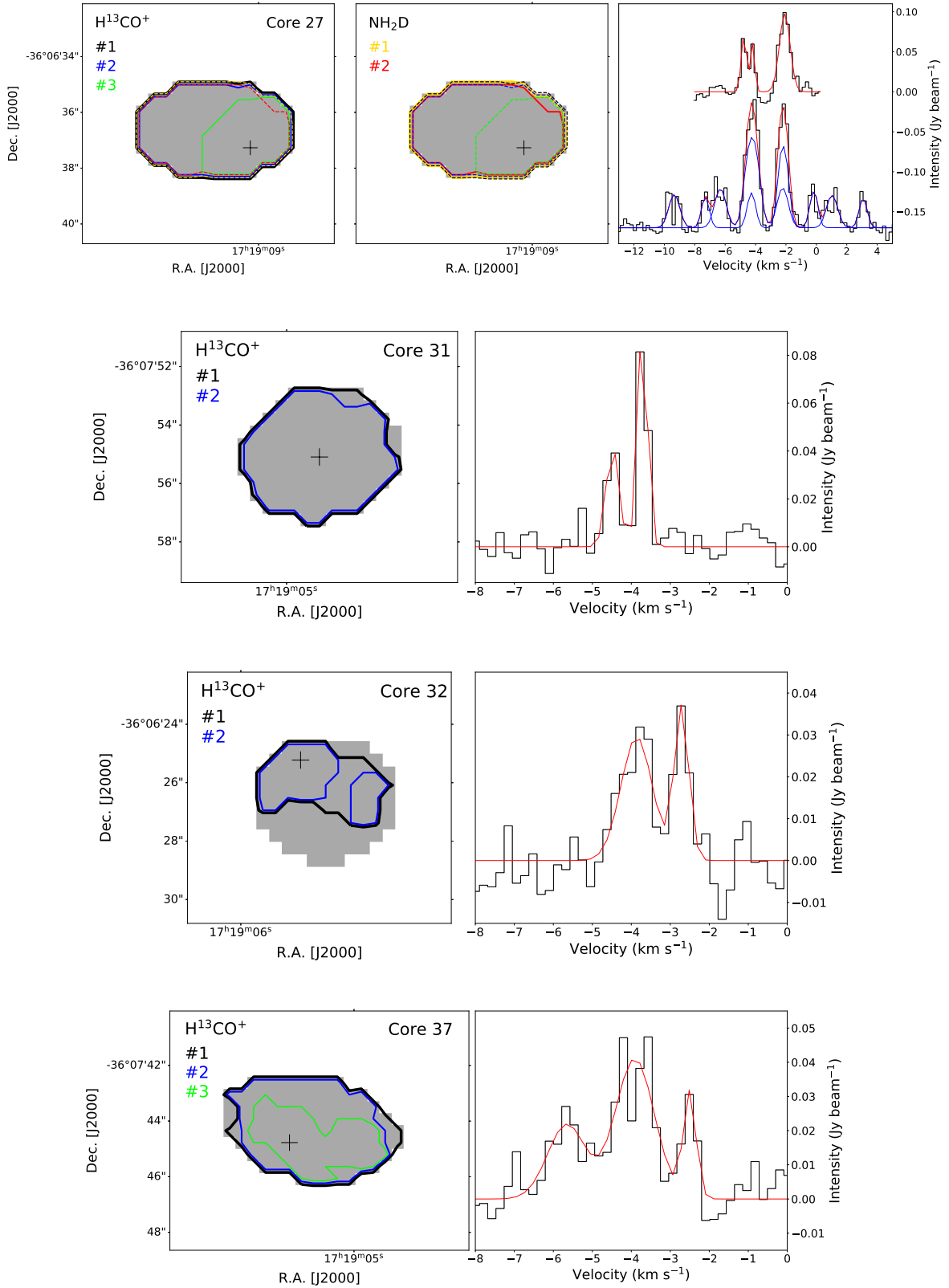
Presented here are individual plots for Figure 8 which are available as the online material. The black cross marks the position of the spectra.



Presented here are individual plots for Figure 8 which are available as the online material.



Presented here are individual plots for Figure 8 which are available as the online material.



Presented here are individual plots for Figure 8 which are available as the online material.

